Structural basis of EHEP-mediated offense against phlorotannin-induced defense from brown algae to protect *aku*BGL activity

Xiaomei Sun[1,¶], Yuxin Ye[1,#a,¶], Naofumi Sakurai[1], Hang Wang[1], Koji Kato[1,#b], Jian Yu[1], Keizo Yuasa[2,#c], Akihiko Tsuji[2], Min Yao[1,*]

[1] Faculty of Advanced Life Science, Hokkaido University, Sapporo, Japan

[2] Graduate School of Bioscience and Bioindustry, Tokushima University, Tokushima, Japan

[#a] Current address: Pingshan translational medicine center, Shenzhen Bay Laboratory, Shenzhen, China

[#b] Current address: Structural Biology Division, Japan Synchrotron Radiation Research Institute (JASRI), Hyogo, Japan

[#c] Current address: Faculty of Science and Engineering, Setsunan University, Neyagawa, Japan

*Corresponding author

E-mail: yao@castor.sci.hokudai.ac.jp (MY)

¶ These authors contributed equally to this work.

Abstract

The defensive-offensive associations between algae and herbivores determine marine ecology. Brown algae utilize phlorotannin as their chemical defense against the predator *Aplysia kurodai*, which uses β-glucosidase (*aku*BGL) to digest the laminarin in algae to glucose. Moreover, *A. kurodai* employs *Eisenia* hydrolysis-enhancing protein (EHEP) as an offense to protect *aku*BGL activity from phlorotannin inhibition by precipitating phlorotannin. To underpin the molecular mechanism of this digestive-defensive-offensive system, we determined the structures of apo and tannic-acid (TNA, a phlorotannin-analog) bound form of EHEP, as well as *aku*BGL. EHEP consisted of three peritrophin-A domains formed in a triangle and bound TNA in the center without significant conformational changes. Structural comparison between EHEP and EHEP–TNA led us to find that EHEP can be resolubilized from phlorotannin-precipitation at an alkaline pH, which reflects a requirement in the digestive tract. *aku*BGL contained two GH1 domains, only one of which conserved the active site. Combining docking analysis, we propose the mechanisms by which phlorotannin inhibits *aku*BGL by occupying the substrate-binding pocket, and EHEP protects *aku*BGL against the inhibition by binding with phlorotannin to free the *aku*BGL pocket.

Introduction

Over millions of years of evolution, predators have successfully coevolved with their prey to maintain an ecological balance [1]. In marine habitats, interactions between algae and marine herbivores dominate marine ecosystems. Most algae are consumed by marine herbivores [2]. They produce secondary metabolites as a chemical defense to protect themselves against predators. The sea hare *Aplysia kurodai*, a marine gastropod, preferentially feeds on the laminarin-abundant brown algae *Eisenia bicyclis* (laminarin constitutes 20%–30% of the dry weight of *E. bicyclis* and acts as a major storage carbohydrate), releasing large amounts of glucose through hydrolysis mediated by 110 and 210 kDa β-glucosidases (*aku*BGLs). Interestingly, such a feeding strategy has attracted attention for producing glucose as a renewable biofuel source [3]. However, to protect themselves against predators, brown algae produce phlorotannin, a secondary metabolite, thereby reducing the digestion of *A. kurodai* by inhibiting the hydrolytic activity of *aku*BGLs. This inhibition has a negative impact on the application of brown algae for producing renewable biofuel sources. As the 110 kDa *aku*BGL is more sensitive to phlorotannin than the 210 kDa BGL [4], we focused on the 110 kDa *aku*BGL in this study (hereafter, *aku*BGL refers to 110 kDa *aku*BGL).

To counteract the antipredator adaptations of algae, herbivores use diverse approaches, such as detoxification, neutralization, defense suppression, and physiological adaptations [5]. *A. kurodai* inhibits the phlorotannin-defense of brown algae through *Eisenia* hydrolysis-enhancing protein (EHEP), a protein from their digestive system that protects *aku*BGL activity from phlorotannin inhibition [4]. Previous studies have shown that incubating *E. bicyclis* with *aku*BGL in the presence of EHEP results in increased glucose production because EHEP binds to phlorotannin and forms an insoluble complex [4].

The *aku*BGL–phlorotannin/laminarin–EHEP system exemplifies the digestion process of *A. kurodai* as well as the defense and antidefense strategies between *E.*

63 *bicyclis* and *A. kurodai*. Although the defense/antidefense strategy has been established,
64 the detailed molecular mechanism of this interplay remains unknown. Further,
65 phlorotannin inhibition hinders the potential application of brown algae as feedstocks
66 for enzymatically producing biofuel from laminarin. Thus, understanding the
67 underlying molecular mechanisms will be beneficial for the application of this system
68 in the biofuel industry.

69 Despite the potential use of laminarin hydrolytic enzymes in the biofuel industry,
70 only a few BGLs of glycoside hydrolases belonging to the GH3 and GH1 family are
71 known to hydrolyze laminarin (e.g., *Talaromyces amestolkiae* BGL[6], *Ustilago*
72 *esculenta* BGL [7], and V*ibrio campbellii* BGL [8] from the GH3 family and
73 *Saccharophagus degradans* 2-40^T BGL [9] from the GH1 family). GH3 is a multidomain
74 enzyme family characterized by N-terminal $(\beta/\alpha)_8$ (NTD) and C-terminal $(\beta/\alpha)_6$ (CTD)
75 domains, with or without auxiliary domains [10]; the nucleophile aspartate and the
76 acid/base glutamate residues exist in the NTD and CTD, respectively. In contrast, the
77 members of the GH1 family generally share a single $(\beta/\alpha)_8$-fold domain (hereafter
78 referred to as GH1 domain [GH1D]), and the two glutamic acid catalytic residues are
79 located in the carboxyl termini of β-strands 4 and 7. Therefore, the two families may
80 use different substrate-recognition and catalytic mechanisms for laminarin. Intriguingly,
81 although *aku*BGL possesses laminarin hydrolytic activity and belongs to the GH1
82 family, its molecular weight is considerably greater than that of other GH1 members.
83 Sequence analysis has indicated that *aku*BGL consists of ≥2 GH1Ds. Because no
84 structural information of BGL active on polysaccharides is available, the catalytic
85 mechanism toward laminarin is unclear.

86 There is limited information on EHEP, a novel cysteine-rich protein (8.2% of the
87 amino acid content), because no structural or functional homologous protein exists in
88 other organisms. EHEP was predicted to consist of three peritrophin-A domains (PADs)
89 with a cysteine-spacing pattern of $CX_{15}CX_5CX_9CX_{12}CX_{5\text{-}9}C$. The PADs consist of
90 peritrophic matrix proteins, which have been proposed to play an important role in

91 detoxifying ingested xenobiotics [11]. For instance, *Aedes aegypti* intestinal mucin 1
92 (*Ae*IMUC1) consists of a signal peptide followed by three PADs with an intervening
93 mucin-like domain; its expression is induced by blood feeding. *Ae*IMUC1-mediated
94 blood detoxification during digestion is completed by binding to toxic heme molecules
95 [12]. Despite the similar domain organization of EHEP and *Ae*IMUC1, their function and
96 binding partner are completely different, implying their different characteristics.
97 However, the characteristics of the EHEP-phlorotannin insoluble complex remain
98 unknown; moreover, it remains unclear why and how EHEP protects *aku*BGL from
99 phlorotannin inhibition.

100 In this study, we determined the structures of apo and tannic acid (TNA,
101 phlorotannin-analog) bound-form of EHEP, as well as *aku*BGL; all isolated from *A.*
102 *kurodai*. The structure of EHEP consists of three PADs arranged in a triangle shape,
103 with TNA bound at the surface of the triangle center. A structural comparison of EHEP
104 and EHEP–TNA revealed no significant changes in conformation upon TNA binding,
105 implying that EHEP maintains its structure when precipitated with TNA. Then, we
106 found the conditions to resolubilize EHEP–TNA precipitate for EHEP recycling. The
107 obtained *aku*BGL structure suggests that only one GH1D (GH1D2) possesses laminarin
108 hydrolytic activity; subsequently, ligand-docking experiments demonstrated that
109 TNA/phlorotannin has a higher binding affinity than laminarin. Our results revealed the
110 mechanisms by which EHEP protects *aku*BGL from phlorotannin inhibition and
111 phlorotannin inhibits the hydrolytic activity of *aku*BGL, providing structural support
112 for the potential application of brown algae for biofuel production.

113 Results

114 Effects of TNA on akuBGL activity with or without EHEP

115 As a chemical defense metabolite of brown algae, phlorotannins are a type of

116 tannins. It is difficult to isolate a compound from phlorotannins because they are a
117 group of polyphenolic compounds with different sizes and varying numbers of
118 phloroglucinol units [13]. Previous studies have reported that the phlorotannin-analog
119 TNA has a comparable inhibition effect on *aku*BGL to that of phlorotannin [4]. Hence,
120 we used TNA instead of a phlorotannin to explore phlorotannin binding with EHEP and
121 *aku*BGL. First, we confirmed TNA inhibition of *aku*BGL activity and clarified the
122 protective effects of EHEP from TNA inhibition. The inhibition experiments showed
123 that the galactoside hydrolytic activity of *aku*BGL decreased with increasing TNA
124 concentration, indicating that TNA inhibits *aku*BGL activity in a dose-dependent
125 manner (Fig. 1A). Approximately 70% *aku*BGL activity was inhibited at a TNA
126 concentration of 40 μM. Moreover, protection ability analysis revealed that EHEP
127 protects *aku*BGL activity from TNA inhibition in a dose-dependent manner, as
128 indicated by the recovery of the inhibited *aku*BGL activity with increasing EHEP
129 concentration (Fig. 1B). Further, approximately 80% of *aku*BGL activity was recovered
130 at an EHEP concentration of 3.36 μM.

131 Overall structure of EHEP

132 Considering the lack of known homologous proteins of EHEP, we determined the
133 structure of natural EHEP using the native-SAD method at a resolution of 1.15 Å, with
134 a R_{work} and R_{free} of 0.18 and 0.19, respectively (Table 1). The residues A21–V227 of
135 A21–K229 in purified EHEP (1–20 aa were cleaved during maturation) were
136 appropriately visualized, whereas two C-terminal residues were disordered. The
137 structure of EHEP consists of three PADs: PAD1 (N24–C79), PAD2 (I92–C146), and
138 PAD3 (F164–C221), which are linked by two long loops, LL1 (Q80–N91) and LL2
139 (R147– G163), and arranged in a triangle shape (Fig. 2A). These three PADs share a
140 similar structure, with a root-mean-squared difference (RMSD) of 1.065 Å over 46 Cα
141 atoms and only ~20.3% sequence identity (Figs. 2B and 2C). The three PADs share a
142 canonical CBM14 fold consisting of two β-sheets containing three N-terminal and two

143 C-terminal antiparallel β-strands. Additionally, two small α-helices were appended to
144 the N- and C-terminus in PAD1 and PAD3 but not in PAD2 (Fig. 2B).
145 Although the Dali server [14] did not provide similar structures using the overall structure
146 of EHEP as the search model, six structures showed similarities with a single PAD of
147 EHEP. These structures were the members of the PAD family, including the chitin-
148 binding domain of chitotriosidase (PDB ID 5HBF) [15], avirulence protein 4 from
149 *Pseudocercospora fuligena* [*Pf*Avr4 (PDB ID 4Z4A)] [16] and *Cladosporium fulvum*
150 [*Cf*Avr4 (PDBID 6BN0)] [17], allergen Der p 23 (PDB ID 4ZCE) [18], tachytitin (PDB ID
151 1DQC) [19], and allergen Blot 12 (PDB ID 2MFK), with Z-scores of 4.7–8.4, RMSD
152 values of 1.2–2.8 Å, and sequence identity of 19%–37%. The highest sequence
153 disparity was detected in PAD2, whereas the greatest structural differences were noted
154 in PAD3. The $C^{No1}X_{15}C^{No2}X_{5}C^{No3}X_{9}C^{No4}X_{12}C^{No5}X_{5\text{-}9}C^{No6}$ motif (superscripts and
155 subscripts indicate the cysteine number and number of residues between adjacent
156 cysteines, respectively) in each PAD of EHEP formed three disulfide bonds between
157 the following pairs: C^{No1}–C^{No3}, C^{No2}–C^{No6}, and C^{No4}–C^{No5} (Fig. 2B). Such rich disulfide
158 bonds may play a folding role in the structural formation of EHEP, with >70% loop
159 conformation. A similar motif with disulfide bonds was observed in tachycitin [19],
160 *Pf*Avr4 [16], *Cf*Avr4 [17], and the chitin-binding domain of chitinase [15]. Although these
161 proteins share a highly conserved core structure, they have different biochemical
162 characteristics. For example, the chitin-binding domain of human chitotriosidase Avr4
163 and tachycitin possess chitin-binding activity, but the critical residues for chitin-binding
164 are not conserved [15, 17, 20], indicating that they employ different binding mechanisms. In
165 contrast, EHEP and allergen Der p 23 do not possess chitin-binding activity [4, 18]. Thus,
166 the PAD family may participate in several biochemical functions.

167 Modification of EHEP

168 Among our structures, the apo structure2 (1.4 Å resolution) clearly showed that the
169 cleaved N-terminus of Ala21 underwent acetylation (Fig. 3A), consistent with the

170 molecular weight results obtained using MALDI–TOF MS [21]. N-terminal acetylation is
171 a common modification in eukaryotic proteins. Such acetylation is associated with
172 various biological functions, such as protein half-life regulation, protein secretion,
173 protein–protein interaction, protein–lipid interaction [22], metabolism, and apoptosis [23].
174 Further, N-terminal acetylation may stabilize proteins [24]. To explore whether
175 acetylation affects the protective effects of EHEP on *aku*BGL, we measured the TNA-
176 precipitating assay of recombEHEP (A21–K229) without acetylation. The results
177 revealed that recombEHEP precipitated after incubation with TNA at a comparable
178 level to that of natural EHEP (Fig. 3B), indicating that acetylation is not indispensable
179 for the phlorotannin binding activity and stabilization of EHEP. Future studies are
180 warranted to verify the exact role of N-terminal acetylation of EHEP in *A.kurodai*.

181 TNA binding to EHEP

182 To understand the mechanism by which TNA binds to EHEP, we determined the
183 structure of EHEP complexed with TNA (EHEP–TNA) using the soaking method. In
184 the obtained structure, both $2F_o–F_c$ and $F_o–F_c$ maps showed an electron density blob of
185 1,2,3,4,6-pentagalloylglucose, a core part of TNA missing the five external gallic acids
186 (Fig. 4A, Fig. S1A). Previous studies have shown that acid catalytic hydrolysis of TNA
187 requires a high temperature of 130°C [25]; even with a polystyrene-hollow sphere catalyst,
188 a temperature of 80°C is required [26]. Therefore, the five gallic acids could not be
189 visualized in the EHEP–TNA structure most likely due to the structural flexibility of
190 TNA.
191 The apo EHEP and EHEP–TNA structures were extremely similar, with an RMSD
192 value of 0.283 Å for 207 Cα atoms (Fig. S1B). However, the superposition of the two
193 structures showed a decrement of the loop part in EHEP–TNA, indicating that EHEP is
194 more stable when bound to TNA. TNA binding caused a slight increase in the α-helix
195 and β-sheet contents of PAD2 and PAD3 (Fig. S1B). In the EHEP–TNA structure, the
196 residues C93–Y96 of PAD2 folded into an α-helix and each β-sheet of the first β-strand

197 in PAD3 elongated by incorporating one residue in the first (G^{176}) and second β-sheets
198 (S^{186}) and three residues in the third β-sheet ($H^{197}MP^{199}$).
199 The EHFP–TNA structure revealed that TNA binds to the center of the triangle formed
200 by the three PADs, a positively charged surface (Fig. 4A and Fig. S1C). The binding
201 pocket on EHEP surface was formed by the C-terminal α-helix of PAD1, the N-terminal
202 α-helix of PAD2, and the middle part (loop) of PAD3 assisted by two long linker loops
203 (LL1 and LL2). TNA was primarily bound to EHEP via hydrogen bonds and
204 hydrophobic interactions (Fig. 4B). Gallic acid1, 4, and 6 interacted with EHEP via
205 hydrogen bonds and additional hydrophobic contacts, whereas gallic acid2 and 3 only
206 hydrophobically interacted with EHEP. The 3-hydroxyl groups of gallic acid1 and 6
207 individually formed a hydrogen bond with the main chain of G74 and the side chain of
208 N75 in PAD1. The backbone carbonyl of Y96 and P199 in PAD2 and PAD3,
209 respectively, formed a hydrogen bond with the 3,5-hydroxyl groups of gallic acid4.
210 Additionally, some hydrogen bonds were formed between TNA and water molecules.
211 TNA binding was also stabilized by hydrophobic interactions between the benzene
212 rings of gallic acid and EHEP. For instance, gallic acid4 and 6 showed alkyl-π
213 interaction with P77 and P201, respectively; moreover, gallic acid3 and 4 formed
214 amide-π stackings with P199.
215 The EHEP–TNA structure clearly showed that TNA binds to EHEP without covalent
216 bonds and the binding does not induce significant structural changes; thus, we
217 attempted to recover EHEP from EHEP–TNA precipitates by adjusting the pH. As
218 hypothesized, re-solubilization of the EHEP–phlorotannin precipitate is pH-dependent
219 (Fig. 4C). The EHEP–TNA precipitate did not resolubilize at pH 7.0; however, after
220 incubating for >1 h at pH 7.5, the precipitate started resolubilizing. Most of the
221 precipitate rapidly resolubilized at an alkaline pH (≥8.0) after incubation for 15 min.
222 Further, the resolubilized EHEP had the same elution profile as that of the natural EHEP
223 (Fig. 4D) in SEC, suggesting that resolubilized EHEP maintained the native structure
224 and its phlorotannin–precipitate activity (Fig. S1E).

225 ## Two domains of *aku*BGL

226 To reveal the structural basis of *aku*BGL recognition of laminarin and inhibition by
227 TNA, we attempted to determine its structure. We soaked crystals in TNA as well as
228 various substrate solutions but finally obtained the optimal resolution using crystal
229 soaking in TNA. There was no blob of TNA in the electron density map of the obtained
230 structure; thus, we considered this structure as the apo form of *aku*BGL.

231 Two *aku*BGL molecules were observed in an asymmetrical unit (MolA and MolB),
232 without the N-terminal 25 residues (M1–D25), as confirmed using N-terminal
233 sequencing analysis of purified natural *aku*BGL. This N-terminal fragment was
234 predicted to be a signal peptide using the web server SignalP-5.0. The residues L26–
235 P978 of L26–N994 were constructed in both MolA and MolB with glycosylation,
236 whereas the remaining C-terminal residues (A979–M994) could not be visualized as
237 they were disordered. The electron density map of Fo–Fc revealed N-glycosylation at
238 three residues, i.e., N113, N212, and N645 (Figs. S2A, B). N-glycosylation of GH
239 enzymes prevents proteolysis and increases thermal stability [27, 28]. Additionally, a study
240 on β-glucosidase *Aspergillus terreus* BGL demonstrated that N-glycosylation of N224
241 affected the folding stability, even when it is located close to a catalytic residue [29]. In
242 *aku*BGL, all N-glycosylation sites were present on the surface, far away from the
243 catalytic site. Therefore, we speculate that *aku*BGL glycosylation does not affect its
244 activity. Except for the difference in visualized glycans resulting from glycosylation,
245 MolA and MolB were similar, with a RMSD value of 0.182 for 899 Ca atoms; therefore,
246 we used MolA for further descriptions and calculations.

247 The structure of *aku*BGL consisted of two independent GH1 domains, GH1D1 (L26–
248 T494) and GH1D2 (D513–P978), linked by a long loop (D495–Y512) (Fig. 5A). There
249 was little interaction between GH1D1 and GH1D2, only in a buried surface area
250 comprising 2% of the total surface (708.9 $Å^2$) (Fig. S2C). GH1D1 and GH1D2 have a
251 sequence identity of 40.47% and high structural similarity with an RMSD value of 0.59

252 Å for 371 Cα atoms (Fig. S3A up).

253 Glucosidases of the GH1 family utilize the retaining mechanism with two glutamic
254 acids for catalyzing glucoside hydrolysis. In general, the distance between the two
255 catalytic oxygen atoms of the side chain of two glutamic acids is approximately 5 Å [30].
256 Sequence and structure alignment of GH1D1 and GH1D2 of *aku*BGL with other
257 members of the GH1 family revealed that the second glutamate is conserved (E404),
258 but the first glutamate is replaced by D192 in GH1D1. The oxygen atoms of the side
259 chains between D192 and E404 of GHD1 were 8.4 Å apart. In contrast, GH1D2
260 conserved two glutamic acids (E675 and E885) at the carboxyl termini of β-strands 4
261 and 7; the distance between oxygen atoms of E675 and E885 side chains was 5.1 Å
262 (Fig. S3A down), similar to that of *Neotermes koshunensis* BGL (*Nk*BGL) [31],
263 *Nannochloropsis oceanica* BGL (*No*BGL) [32], and *Spodoptera frugiperda* BGL (3.9–
264 4.9Å) [33]. Furthermore, regarding the two other conserved essential regions for β-
265 glucosidase activity, namely, glycone-binding site (GBS) and catalysis-related residues
266 (CR), GH1D1 conserved neither GBS nor CR, whereas GH1D2 conserved both (Fig.
267 5B). Altogether, we suggest that GH1D1 does not possess catalytic activity. We
268 expressed and purified the recombinant GH1D1, which did not show any hydrolytic
269 activity toward O-PNG (Figs. S2D, E), although we could not rule out the effect of N-
270 glycosylation.

271 A multi-GH1D assembly has been reported in β-glucosidase *Cj*CEL1A of *Corbicula*
272 *japonica* and glycosidase *LpM*DGH1 of the shipworm *Lyrodus pedicellatus*.
273 *Lp*MDGH1 has both exo- and endo-glucanase activity and is possibly implicated in
274 cellulose and hemicellulose digestion. *Cj*CEL1A has two tandem GH1Ds with a
275 sequence identity of 43.41% [34]. Two catalytic glutamic acids and the residues related to
276 substrate binding are conserved in the second GH1D, whereas the first GH1 domain
277 lacks these conserved residues and may play a role in folding the catalytic domain.
278 *LpM*DGH1 consists of six GH1Ds, among which GH1D2, 4, 5, and 6 contain the
279 conserved residues for activity, whereas others do not contain these residues and might

280 be involved in protein folding or substrate interactions [35].

281 Structural comparison of GH1D2 with other BGLs, including *Nk*BGL, rice (*Oryza*
282 *sativa L.)* BGL (*Os*BGL), and microalgae *No*BGL, revealed the characteristics of each
283 active pocket (Fig. S3B). *Os*BGL and *No*BGL have a deep, narrow, and straight pocket,
284 whereas GH1D2 and *Nk*BGL have a broad and crooked pocket. Such active pocket
285 shapes reflect the substrate preferences of *Os*BGL and *No*BGL; they hydrolyze
286 laminaribiose with no detectable activity toward laminaritetraose [32, 36]. Furthermore,
287 the difference in the features of large active pockets between *Nk*BGL and GH1D2,
288 wherein GH1D2 often possesses an auxiliary site with several aromatic residues bound
289 to the carbohydrate via CH-π interactions [37], may explain their substrate specificity.
290 *Nk*BGL efficiently hydrolyzes laminaribiose and cellobiose but has weak hydrolytic
291 activity toward laminarin [38]. In contrast, the GH1D2 of *aku*BGL has similar activity
292 levels toward cellobiose and laminarin [39]. Therefore, the GH1D2 of *aku*BGL may
293 recognize larger substrates than that of other BGLs. Laminarin typically has a curved
294 conformation; accordingly, narrow- and straight-shaped pockets are incompatible for
295 binding. Furthermore, we docked GH1D2 with laminaritetraose, wherein the four
296 glucose units formed extensive contacts with GH1D2. Hydrogen bonds involved the
297 catalytic residues E675 and E885. In addition, several aromatic residues, such as F677,
298 F689, Y819, W857, and W935, formed π-π stacking (Fig. S4). Some interacting
299 residues belonged to GBS and CR sites, such as E675, Y819, E885, and W935.
300 Additionally, the docking structure revealed that the +4 glucose of laminaritetraose is
301 located at the auxiliary binding site and that atom O1 of the +4 glucose is positioned
302 outside the pocket (Fig. S4), implying that the auxiliary binding site with several
303 aromatic residues (F677, W681, and F689) of GH1D2 facilitates laminarin binding.

304 Inhibitor binding of *aku*BGL

305 As we could not obtain the complex structure of *aku*BGL with TNA, we performed
306 docking calculations of *aku*BGL GH1D2 with TNA to explore the inhibition

307 mechanism. The docking model of *aku*BGL–TNA showed that seven gallic acid rings
308 of TNA formed an extensive hydrogen bond network with *aku*BGL in the binding
309 pocket (Fig. 6). The hydroxyl groups of TNA formed hydrogen bonds with the residues
310 N552, E675, D735, K739, K759, Q840, T844, D852, and K859 of GH1D2. Moreover,
311 benzene rings showed hydrophobic interactions with several hydrophobic residues. In
312 particular, stable π-π stacking was observed between TNA and residues F547, W631,
313 F689, Y846, W857, and W935. Among these residues, the conserved E675 was the
314 catalytic residue, and W631, W935, and E934 contributed to GBS and CR sites.
315 In addition, we performed a docking calculation of GH1D2 with the characteristic
316 inhibitors eckol and phloroglucinol [40]. The binding mechanisms of eckol and
317 phloroglucinol were similar to those of TNA but with different contact residues (Fig.
318 S5). For eckol, the six hydroxyl groups formed hydrogen bonds with residues E675,
319 D735, E737, K759, E885, and E934. Additionally, residues W631, F677, F689, Y819,
320 W857, W935, F943, and W927 formed π-π stacking with eckol. For phloroglucinol, the
321 three hydroxyl groups formed hydrogen bonds with E675, E885, and E934, whereas
322 residues W631, F689, Y819, W857, W935, and W927 formed π-π stacking with the
323 benzene ring.
324 In summary, the three inhibitors inhibited *aku*BGL activity through similar binding
325 mechanisms to occupy the substrate-binding site, suggesting a reversible competitive
326 inhibition mechanism. The docking scores of the inhibitors TNA, eckol, and
327 phloroglucinol were −8.8, −7.3, and −5.7 kcal/mol, respectively, whereas the substrate
328 laminaritetraose had a docking score of −6.6 kcal/mol. TNA binding and phloroglucinol
329 had the highest and lowest negative docking score, respectively, indicating that TNA
330 has a higher binding affinity to *aku*BGL. This finding is consistent with that of a
331 previous study showing that phloroglucinol binding has a weaker inhibitory activity
332 than TNA [4].

333 # Discussion

334 In marine habitats, the ecological interactions between brown algae and herbivores
335 dominate marine ecosystems [41]. The *aku*BGL–phlorotannin/laminarin–EHEP system
336 represents the feeding defense-offense associations between *A. kurodai* and brown
337 algae. We focused on this system to understand the molecular mechanism at the atomic
338 level. In contrast to most GH1 BGLs containing one catalytic GH1 domain, *aku*BGL
339 consists of noncatalytic GH1D1 and catalytic GH1D2. The noncatalytic GH1D1 may
340 act as a chaperone of GH1D2, as we successfully overexpressed GH1D1 but failed to
341 do the same for GH1D2. A similar function has been suggested in *Cj*CEL1A [34] and
342 *LpM*DGH1 [35].

343 BGLs have different substrate preferences in the degree of polymerization and
344 type of glycosidic bond. In general, BGLs prefer to react with mono-oligo sugars over
345 polysaccharides. For instance, *Os*BGL, *No*BGL, and *Nk*BGL hydrolyze disaccharides
346 (cellobiose and laminaribiose) but display no or weak activity toward polysaccharides
347 (cellulose and laminarin) [32, 36, 38]. The structure of GH1D2 explained the substrate
348 preference for the polysaccharide laminarin. GH1D2 contains an additional auxiliary
349 site composed of aromatic residues (Fig. S3B) in the substrate entrance pocket, which
350 enables it to accommodate a long substrate, contributing to *aku*BGL activity toward
351 laminarin, as supported by docking calculations (Fig. S4). In addition, docking analysis
352 of *aku*BGL GH1D2 with inhibitors (TNA, phlorotannin, eckol, and phloroglucinol)
353 revealed that these inhibitors bound to the substrate-binding site via hydrogen bonds
354 and hydrophobic interactions similar to laminarin. Such binding mechanisms suggest
355 the presence of competitive inhibition to occupy the binding site, consistent with
356 previous research [4].

357 EHEP, expressed in the midgut of *A. kurodai*, was identified as an antidefense
358 protein, protecting the hydrolysis activity of *aku*BGL from phlorotannin inhibition [4].
359 Such an ecological balance also exists between plants and their predator mammals and

360 insects. Similar to brown algae, plants use the toxic secondary metabolite tannins as
361 their defense mechanism against predators, which constitute 5%–10% of dry weight of
362 leaves. In vertebrate herbivores, tannins reduce protein digestion. In phytophagous
363 insects, tannins may be oxidized at an alkaline pH of insect midgut and cause damage
364 to cells. The evolution of plant-herbivore survival competition has led to the
365 development of remarkably unique adaptation strategies. Mammals feeding on plants
366 that contain tannin may overcome this defense by producing tannin-binding proteins,
367 proline-rich proteins, and histatins [42]. Proline constitutes at least 20% of the total amino
368 acid content in proline-rich proteins; for some species, the proportion of proline reaches
369 40%. Histidine constitutes 25% of total amino acid content in histatins. Both proline-
370 rich proteins and histatins are nonstructural proteins in solution. In caterpillars, the
371 oxidation damage of tannin is reduced by the low oxygen level. Some insects use the
372 peritrophic membrane to transport tannins into the hemolymph, where they are excreted
373 [43]. Additionally, the peritrophic envelop protects insects from tannins by forming an
374 impermeable barrier to tannins [44]. *A. kurodai* uses a similar strategy with mammals by
375 secreting the tannin-binding protein EHEP. Although EHEP has a completely different
376 amino acid composition with proline-rich proteins and histatins, EHEP also binds to
377 phlorotannin. Therefore, EHEP may be a specific counteradaptation that allows
378 *A.kurodai* to feed on brown algae, as there are no homologous proteins in other
379 organisms.

380 The three PADs of EHEP are arranged in a triangle shape, forming a large cavity on
381 the surface at the triangle center to provide a ligand-binding site. Interestingly, EHEP–
382 TNA crystal packing revealed that each TNA simultaneously binds to three EHEP
383 molecules and crosslinks them together (Fig. S1D); this may be responsible for EHEP
384 precipitation by TNA. EHEP has a positively charged surface at a pH of <6.0, whereas
385 the surface becomes negatively charged at a pH of >7.0 (Fig. S1C). Meanwhile, TNA
386 has a pKa of 4.9–8 [45-47], showing minor negative charges at an acidic pH and the highest
387 negative charge at a pH of >7.0 [48]. Therefore, TNA binds to EHEP at a pH of <6.0 (pH

388 of crystallization = 4.5), but it shows charge repulsion with EHEP at a pH of >8.0.
389 Altogether, TNA is protonated and behaves as a hydrogen bond donor when the pH is
390 below its pKa, whereas when the pH is above its pKa, TNA is deprotonated and the
391 hydrogen bonding cannot be maintained. As losing hydrogen bonds and increasing
392 repulsive forces at a pH >8.0, the precipitated EHEP–TNA could not dissolve in the
393 buffer of pH > 8.0. This pH-induced reversible interaction also occurred in other
394 proteins, such as BSA, pepsin, and cytochrome C [49]. The phlorotannin members share
395 a similar structure with TNA; thus, we speculate that the EHEP–phlorotannin complex
396 also exhibits a pH-induced reversible interaction. *In vivo*, the pH of the digestive fluid
397 of *A. kurodai* is approximately 5.5, which favors the binding of EHEP to phlorotannin.
398 In the alkaline hindgut [50], the EHEP–phlorotannin disassociates (Fig. 7), and the
399 phlorotannin is subsequently excreted from the anus.

400 Based on the EHEP–TNA structure and docking models of *aku*BGL-
401 inhibitor/substrate, we proposed a mechanism of phlorotannin inhibition on *aku*BGL
402 activity and EHEP protection from phlorotannin inhibition (Fig. 7). Because laminarin
403 lacks the benzene rings essentially to forming π-stacking interactions with EHEP, the
404 EHEP can be considered no binding with the laminarin. In the absence of EHEP,
405 phlorotannin occupies the substrate-binding site of *aku*BGL, inhibiting the substrate
406 from entering the activity pocket and resulting in no glucose production. In the presence
407 of EHEP, it competitively binds to phlorotannin, freeing the *aku*BGL pocket. Then, the
408 substrate can enter the active pocket of *aku*BGL and glucose can be produced normally.
409 The digestive fluid of *A. kurodai* contains EHEP at a high concentration (>4.4 μM) [4],
410 which is slightly higher than the concentration of EHEP (3.36 μM) that protects
411 *aku*BGL activity (Fig. 1B). The high concentration of EHEP allows *A. kurodai* feeding
412 of phlorotannin-rich brown algae. The balance between phlorotannin inhibition and
413 protection is controlled by the concentrations of phlorotannin and EHEP *in vivo*.

414 The *aku*BGL–phlorotannin/laminarin–EHEP system is the digestive-defensive-
415 offensive associations between algae and herbivores. Our study presented the molecular

416 mechanism of this system at the atomic level, providing a molecular explanation for
417 how the sea hare *A. kurodai* utilizes EHEP to protect *aku*BGL activity from
418 phlorotannin inhibition. Further, such a feeding strategy has attracted attention for
419 producing glucose as a renewable biofuel source, so our studies provide a molecular
420 basis for the biofuel industry applications of brown algae.

421 Materials and Methods

422 EHEP and *aku*BGL preparation

423 Natural EHEP (22.5 kDa) and *aku*BGL (110 kDa) were purified from *A. kurodai*
424 digestive fluid as described previously [4]. For crystallization, we further added one step
425 purification of EHEP using size exclusion chromatography (HiLoad 16/60 Superdex
426 75, GE Healthcare), for which the column was equilibrated with 20 mM MES–NaOH
427 buffer (pH 6.5). Obtained EHEP was then concentrated to 15–25 mg/mL using
428 Vivaspin-4 10K columns (Sartorius, Göttingen, Germany). About *aku*BGL, we
429 exchanged buffer from 20 mM Tris-HCl pH 7.0 to 20 mM Bis-tris pH 6.0 and
430 concentrated it to 11 mg/mL using Amicon with a cutoff of 50 kDa.
431 To verify whether chemical modifications which was indicated by previous study (13)
432 affect the function of EHEP, we prepared recombinant EHEP (recombEHEP) without
433 the N-terminal signal peptide (1–20 aa) and chemical modifications [21]. EHEP cDNA
434 was obtained via reverse transcription–polymerase chain reaction (RT–PCR) using the
435 total RNA of *A. kurodai* as a template. The reamplified fragment was digested and
436 ligated to a plasmid derived from pET28a (Novagene, Darmstadt, Germany). We

437 transformed the plasmid containing recombEHEP into *E. coli* B834(DE3) pARE2 and
438 expressed it with a C-terminal hexahistidine-tag. The cells were cultured in lysogeny
439 broth (LB) medium with the antibiotics kanamycin (25 mg/L) and chloramphenicol (34
440 mg/L) until the optical density at 600 nm (OD_{600}) reached 0.6. Subsequently,
441 overexpression was induced by adding 0.5 mM isopropyl b-D-L-thiogalactopyranoside
442 for 20 h at 20 °C. After harvesting by centrifugation, the cells were resuspended in a
443 buffer containing 50 mM Tris–HCl pH 7.4, 300 mM NaCl, DNase, and lysozyme and
444 were disrupted via sonication. The insoluble part was removed by centrifugation for 30
445 min at 40000 ×*g* at 4 °C. We loaded the supernatant onto a 5-mL Histrap HP column
446 and the recombEHEP was eluted using increasing concentrations of imidazole (0–500
447 mM). The purified proteins were dialyzed against a solution containing 50 mM Tris–
448 HCl pH 7.4 and 50 mM NaCl and subsequently loaded onto a Hitrap Q column and
449 eluted by a linear gradient of a solution containing 50 mM Tris–HCl and 1 M NaCl.
450 Fractions containing recombEHEP were concentrated and further purified using a gel
451 filtration column (Hiload 16/60 superdex 75 pg) equilibrated with 20 mM sodium
452 acetate pH 6.0 and 100 mM NaCl. We collected the fractions containing recombEHEP
453 and concentrated them to 2.1 mg/mL using Amicon (Merck, American).
454

455 **TNA binding assay for recombEHEP**

456 We measured the binding activity of recombEHEP using precipitation analysis method,

457 as described previously [4]. Briefly, recombEHEP was incubated with TNA at 25 °C for
458 90 min and centrifuged for 10 min at 12000 ×*g* at 4 °C. Then, we washed the precipitates
459 twice and resuspended them in an SDS–PAGE loading buffer for binding analysis.

460 Effects of TNA on *aku*BGL activity with or without EHEP

461 Ortho-nitrophenyl-β-galactoside (ONPG) was used as a substrate to measure *aku*BGL
462 activity. The reaction system (100μL) included 2.5 mM ONPG, 49 nM *aku*BGL, and
463 different TNA concentrations in a reaction buffer (50 mM CH_3COONa pH 5.5, 100 mM
464 NaCl, and 10 mM $CaCl_2$). After incubation for 10 min at 37 °C, 100 μL of methanol
465 was added to each sample to terminate the reaction. Then, the mixture was centrifuged
466 for 10 min at 15000 ×*g* at 4 °C and the supernatant was used for analyzing *aku*BGL
467 activity via HPLC. To measure the protective effect of EHEP on *aku*BGL, we added
468 different amounts of EHEP to the reaction system.

469 Resolubilization of the EHEP–eckol precipitate

470 A mixture of 2 mg of EHEP and 0.4 mg of eckol was incubated at 37 °C for 1 h,
471 followed by centrifugation at 12000 ×g for 10 min, and the supernatant was removed.
472 The sediment was dissolved in 50 mM Tris–HCl buffer at different pH (7.0–9.0) and
473 the absorbance at 560 nm was measured over time.

474 Crystallization and data collection

475 The crystallization, data collection, and initial phase determination of EHEP were

476 described previously [21]. As EHEP precipitates when bound to TNA, we could not
477 cocrystallize EHEP with TNA. Therefore, we used the soaking method to obtain the
478 EHEP–TNA complex. Owing to the poor reproducibility of EHEP crystallization, we
479 used a co-cage-1 nucleant [51] to prepare EHEP crystals for forming the complex with
480 TNA. Finally, we obtained high-quality EHEP crystals under the reservoir solution
481 containing 1.0 M sodium acetate, 0.1 M imidazole (pH 6.5) with co-cage-1 nucleant.
482 Subsequently, we soaked the EHEP crystals in a reservoir solution containing 10 mM
483 TNA at 37 °C for 2 days; further, they were maintained at 20 °C for 2 weeks. Next, we
484 soaked the EHEP crystals in a reservoir solution containing 10 mM phloroglucinol. For
485 data collection, the crystal was soaked in a cryoprotectant solution containing 20% (v/v)
486 glycerol along with the reservoir solution. Diffraction data were collected under a cold
487 nitrogen gas stream at 100 K using Photon Factory BL-17 (Tsukuba, Japan) or Spring
488 8 BL-41XU (Hyogo, Japan).
489 For *aku*BGL crystallization, the initial crystallization screening was performed using
490 the sitting-drop vapor-diffusion method with Screen classics and Classics II
491 crystallization kits (Qiagen, Hilden, Germany) and PACT kits (Molecular Dimensions,
492 Anatrace, Inc.) at 20 °C. Crystallization drops were set up by mixing 0.5 μL of protein
493 solution with an equal volume of the reservoir solution. The initial crystals were
494 obtained under condition no. 41 (0.1 M sodium acetate pH 4.5 and 25% polyethylene
495 glycol [PEG] 3350) of Classics II, no. 13 (0.1 M MIB buffer [25 mM sodium malonate
496 dibasic monohydrate, 37.5 mM imidazole, and 37.5 mM boric acid], with pH 4.0 and

497 25% PEG 1500), and no. 37 (0.1 M MMT buffer [20 mM DL-malic acid, 40 mM MES
498 monohydrate, and 40 mM Tris], with pH 4.0 and 25% PEG 1500) of PACT. After
499 optimization by varying the buffer pH and precipitant concentration and adding co-
500 cage1 nucleant, the optimal crystals were obtained using 0.1 M sodium acetate pH 4.5,
501 and 20% PEG 3350 with a co-cage1 nucleant at a protein concentration of 5.4 mg/mL.
502 Diffraction data were collected under a cold nitrogen gas stream at 100 K using Photon
503 Factory BL-1A (Tsukuba, Japan) after cryoprotection by adding glycerol to a 20% final
504 concentration into the reservoir solution. The optimal resolution of diffraction data was
505 obtained by soaking a crystal with 5 mM TNA in the reservoir buffer at 37 °C for 4 h.
506 All datasets were indexed, integrated, scaled, and merged using *XDS/XSCALE* program
507 [52]. Statistical data collection and process are summarized in Table 1.

508 Structure determination and refinement

509 For EHEP structure determination, after initial phasing via the native-SAD method[21,
510 53], the model was obtained and refined with *auto-building* using *Phenix.autobuil* of
511 *Phenix* software suite [54]. The obtained native-SAD structure was used as a model for
512 rigid body refinement using *phenix.refine* [55] of *Phenix* software suite with a native data
513 at high resolution of 1.15 Å. The structure of EHEP was automatically rebuilt using
514 *Phenix.autobuil* of the *Phenix* software suite again [54]. Several rounds of refinement
515 were performed using *Phenix.refine* of the *Phenix* software suite [54], alternating with
516 manual fitting and rebuilding using *COOT* program [56]. The final refinement statistics

517 and geometry are shown in Table 1.

518 The structure of the EHEP–TNA complex was determined via the molecular
519 replacement (MR) method using the EHEP structure as a search model with *Phaser*
520 of *Phenix* software suite [57]. The electron density block of TNA was clearly shown in
521 both $2F_o–F_c$ and $F_o–F_c$ maps. Subsequently, TNA structure was manually constructed,
522 followed by several rounds of refinement using *Phenix.refine* [54], with manual fitting
523 and rebuilding using *COOT* [56]. We also determined the structure of phloroglucinol-
524 soaked crystals at a resolution of 1.4 Å via the MR method using the refined EHEP
525 structure as a search model with *Phaser*, but no electron density block of phloroglucinol
526 was obtained. Therefore, we referred to this structure as the apo form (apo structure2).
527 The final refinement statistics and geometry are shown in Table 1.

528 We determined the structure of *aku*BGL via the MR method using *Phaser* of *Phenix*
529 software suite [57]. We used one GH domain (86–505 aa) of β-klotho (PDB entry: 5VAN)
530 [58] as the search model. This GH domain of β-klotho shares 30% sequence identity with
531 *aku*BGL. Four GH domains of two molecules in an asymmetric unit were found and
532 subsequently rebuilt with *Phenix_autobuild* of *Phenix* software suite [54]. Finally,
533 refinement of *aku*BGL structure was performed as described for EHEP.

534 Docking studies of *aku*BGL with phlorotanins and laminarins

535 We used Schrodinger Maestro program for performing docking studies [59]. First, we
536 superimposed the structure of *Os*BGL mutant complexed with cellotetraose (PDB ID

537 4QLK) to that of *aku*BGL GH1D2 to define the ligand position in the ligand-binding
538 cavity. Then, we modified the structure of the *aku*BGL GH1D2 using wizard module
539 to remove water molecules and add hydrogen atoms for docking. The 2D structures of
540 the inhibition ligands, including TNA, phloroglucinol, and eckol, were downloaded
541 from Pubchem [60] and further converted to 3D structures using the LigPrep module of
542 Schrodinger Maestro program. The structure of the substate laminaritetraose was
543 extracted from the *Zobellia galactanivorans* β-glucanase–laminaritetraose complex
544 structure (PDB ID: 4BOW) [61]. Then, a receptor grid was constructed in the center of
545 the ligand-binding cavity. We performed docking using the Glide standard precision
546 mode without any constraints. The optimal binding pose was determined using the
547 lowest Glide score, and docked structures were analyzed using PyMol.

548 **Data Availability**

549 The atomic coordinates were deposited in the PDB with the accession codes as follows:
550 EHEP with 1.15 Å resolution (8IN3), EHEP with 1.4 Å resolution (8IN4), EHEP
551 complexed with tannic acid (8IN6), *aku*BGL(8IN1).
552

553 **Acknowledgments**

554 This work was supported in part by Grant-in-Aid for Scientific Research (B)
555 (Grant Number 21H01754 To M. Y) and Platform Project for Supporting Drug
556 Discovery and Life Science Research (Basis for Supporting Innovative Drug Discovery
557 and Life Science Research (BINDS)) from Japan Agency for Medical Research and

558 Development (AMED) under Grant Number JP18am0101071 and JP19am0101083.
559 We are grateful to the Photon Factor and SPring-8 (No. 2017B2545, 2017A2551,
560 2018B2538) for beam time and the beamline staff for their assistance for data collection.
561

562 # References

563 1. Becklin, K.M. A Coevolutionary Arms Race: Understanding Plant-Herbivore
564 Interactions. *The American Biology Teacher* **70**, 288-292 (2008).
565 2. Jormalainen, V. & Honkanen, T. in Algal Chemical Ecology 57-89 (2008).
566 3. Enquist-Newman, M. et al. Efficient ethanol production from brown
567 macroalgae sugars by a synthetic yeast platform. *Nature* **505**, 239-243 (2014).
568 4. Tsuji, A., Kuwamura, S., Shirai, A. & Yuasa, K. Identification and
569 Characterization of a 25 kDa Protein That Is Indispensable for the Efficient
570 Saccharification of Eisenia bicyclis in the Digestive Fluid of Aplysia kurodai.
571 *PLoS One* **12**, e0170669 (2017).
572 5. Erb, M. & Reymond, P. Molecular Interactions Between Plants and Insect
573 Herbivores. *Annu Rev Plant Biol* **70**, 527-557 (2019).
574 6. Mendez-Liter, J.A., de Eugenio, L.I., Prieto, A. & Martinez, M.J. The beta-
575 glucosidase secreted by Talaromyces amestolkiae under carbon starvation: a
576 versatile catalyst for biofuel production from plant and algal biomass.
577 *Biotechnol Biofuels* **11**, 123 (2018).
578 7. Nakajima, M., Yamashita, T., Takahashi, M., Nakano, Y. & Takeda, T.

579 Identification, cloning, and characterization of beta-glucosidase from Ustilago
580 esculenta. *Appl Microbiol Biotechnol* **93**, 1989-1998 (2012).
581 8. Wang, Z. et al. A novel Vibrio beta-glucosidase (LamN) that hydrolyzes the
582 algal storage polysaccharide laminarin. *FEMS Microbiol Ecol* **91**, fiv087 (2015).
583 9. Kim, D.H., Kim, D.H., Lee, S.H. & Kim, K.H. A novel beta-glucosidase from
584 Saccharophagus degradans 2-40(T) for the efficient hydrolysis of laminarin
585 from brown macroalgae. *Biotechnol Biofuels* **11**, 64 (2018).
586 10. Mohsin, I., Poudel, N., Li, D.C. & Papageorgiou, A.C. Crystal Structure of a
587 GH3 beta-Glucosidase from the Thermophilic Fungus Chaetomium
588 thermophilum. *Int J Mol Sci* **20** (2019).
589 11. Hegedus, D., Erlandson, M., Gillott, C. & Toprak, U. New Insights into
590 Peritrophic Matrix Synthesis, Architecture, and Function. *Annual Review of*
591 *Entomology* **54**, 285-302 (2009).
592 12. Devenport, M. et al. Identification of the Aedes aegypti peritrophic matrix
593 protein AeIMUCI as a heme-binding protein. *Biochemistry* **45**, 9540-9549
594 (2006).
595 13. Cassani, L. et al. Seaweed-based natural ingredients: Stability of phlorotannins
596 during extraction, storage, passage through the gastrointestinal tract and
597 potential incorporation into functional foods. *Food Res Int* **137**, 109676 (2020).
598 14. Holm, L. & Rosenstrom, P. Dali server: conservation mapping in 3D. *Nucleic*
599 *Acids Res* **38**, W545-549 (2010).

600 15. Fadel, F. et al. X-Ray Crystal Structure of the Full Length Human
601 Chitotriosidase (CHIT1) Reveals Features of Its Chitin Binding Domain. *PLoS*
602 *One* **11**, e0154190 (2016).
603 16. Kohler, A.C. et al. Structural Analysis of an Avr4 Effector Ortholog Offers
604 Insight into Chitin Binding and Recognition by the Cf-4 Receptor. *Plant Cell*
605 **28**, 1945-1965 (2016).
606 17. Hurlburt, N.K., Chen, L.H., Stergiopoulos, I. & Fisher, A.J. Structure of the
607 Cladosporium fulvum Avr4 effector in complex with (GlcNAc)6 reveals the
608 ligand-binding mechanism and uncouples its intrinsic function from recognition
609 by the Cf-4 resistance protein. *PLoS Pathog* **14**, e1007263 (2018).
610 18. Mueller, G.A. et al. Serological, genomic and structural analyses of the major
611 mite allergen Der p 23. *Clin Exp Allergy* **46**, 365-376 (2016).
612 19. Suetake, T. et al. Chitin-binding proteins in invertebrates and plants comprise a
613 common chitin-binding structural motif. *J Biol Chem* **275**, 17929-17932 (2000).
614 20. Madland, E., Crasson, O., Vandevenne, M., Sorlie, M. & Aachmann, F.L. NMR
615 and Fluorescence Spectroscopies Reveal the Preorganized Binding Site in
616 Family 14 Carbohydrate-Binding Module from Human Chitotriosidase. *ACS*
617 *Omega* **4**, 21975-21984 (2019).
618 21. Sun, X. et al. Crystallographic analysis of Eisenia hydrolysis-enhancing protein
619 using a long wavelength for native-SAD phasing. *Acta Crystallographica*
620 *Section F-Structural Biology Communications* **76**, 20-24 (2020).

621 22. Silva, R.D. & Martinho, R.G. Developmental roles of protein N-terminal
622 acetylation. *Proteomics* **15**, 2402-2409 (2015).
623 23. Hollebeke, J., Van Damme, P. & Gevaert, K. N-terminal acetylation and other
624 functions of Nalpha-acetyltransferases. *Biol Chem* **393**, 291-298 (2012).
625 24. Lange, P.F. & Overall, C.M. TopFIND, a knowledgebase linking protein termini
626 with function. *Nat Methods* **8**, 703-704 (2011).
627 25. Jie Fu, J.x., Zhang, Y. & Lu, X. A Greener Process for Gallic Acid Production
628 from Tannic Acid Hydrolysis with Hydrochloric Acid. *Asian Journal of*
629 *Chemistry* **27**, 3328-3332 (2015).
630 26. Luo, Q. et al. A novel green process for tannic acid hydrolysis using an
631 internally sulfonated hollow polystyrene sphere as catalyst. *RSC Advances* **8**,
632 17151-17158 (2018).
633 27. Amore, A. et al. Distinct roles of N- and O-glycans in cellulase activity and
634 stability. *Proc Natl Acad Sci U S A* **114**, 13667-13672 (2017).
635 28. Han, C. et al. Improvement of the catalytic activity and thermostability of a
636 hyperthermostable endoglucanase by optimizing N-glycosylation sites.
637 *Biotechnol Biofuels* **13**, 30 (2020).
638 29. Wei, W. et al. N-glycosylation affects the proper folding, enzymatic
639 characteristics and production of a fungal beta-glucosidas. *Biotechnol Bioeng*
640 **110**, 3075-3084 (2013).
641 30. Hayashi, Y. et al. Klotho-related protein is a novel cytosolic neutral beta-

642 glycosylceramidase. *J Biol Chem* **282**, 30889-30900 (2007).

643 31. Jeng, W.Y. et al. High-resolution structures of Neotermes koshunensis beta-
644 glucosidase mutants provide insights into the catalytic mechanism and the
645 synthesis of glucoconjugates. *Acta Crystallogr D Biol Crystallogr* **68**, 829-838
646 (2012).

647 32. Dong, S. et al. Structural insight into a GH1 beta-glucosidase from the
648 oleaginous microalga, Nannochloropsis oceanica. *Int J Biol Macromol* **170**,
649 196-206 (2021).

650 33. Tamaki, F.K. et al. Using the Amino Acid Network to Modulate the Hydrolytic
651 Activity of beta-Glycosidases. *PLoS One* **11**, e0167978 (2016).

652 34. Sakamoto, K., Uji, S., Kurokawa, T. & Toyohara, H. Molecular cloning of
653 endogenous beta-glucosidase from common Japanese brackish water clam
654 Corbicula japonica. *Gene* **435**, 72-79 (2009).

655 35. Sabbadin, F. et al. Uncovering the molecular mechanisms of lignocellulose
656 digestion in shipworms. *Biotechnol Biofuels* **11**, 59 (2018).

657 36. Opassiri, R. et al. Characterization of a rice β-glucosidase highly expressed in
658 flower and germinating shoot. *Plant Science* **165**, 627-638 (2003).

659 37. Hudson, K.L. et al. Carbohydrate-Aromatic Interactions in Proteins. *J Am Chem*
660 *Soc* **137**, 15152-15160 (2015).

661 38. Ni, J., Tokuda, G., Takehara, M. & Watanabe, H. Heterologous expression and
662 enzymatic characterization of .BETA.-glucosidase from the drywood-eating

termite, Neotermes koshunensis. *Applied Entomology and Zoology* **42**, 457-463 (2007).

39. Tsuji, A., Tominaga, K., Nishiyama, N. & Yuasa, K. Comprehensive enzymatic analysis of the cellulolytic system in digestive fluid of the Sea Hare Aplysia kurodai. Efficient glucose release from sea lettuce by synergistic action of 45 kDa endoglucanase and 210 kDa ss-glucosidase. *PLoS One* **8**, e65418 (2013).

40. Jung, H.A., Oh, S.H. & Choi, J.S. Molecular docking studies of phlorotannins from Eisenia bicyclis with BACE1 inhibitory activity. *Bioorg Med Chem Lett* **20**, 3211-3215 (2010).

41. Amsler, C.D. & Fairhead, V.A. in Advances in Botanical Research, Vol 43: Incorporating Advances in Plant Pathology, Vol. 43. (ed. J.A. Callow) 1-91 (2006).

42. Shimada, T. Salivary proteins as a defense against dietary tannins. *J Chem Ecol* **32**, 1149-1163 (2006).

43. War, A.R. et al. in Co-Evolution of Secondary Metabolites 795-822 (2020).

44. Barbehenn, R.V. & Peter Constabel, C. Tannins in plant-herbivore interactions. *Phytochemistry* **72**, 1551-1565 (2011).

45. Lin, D. et al. The effect of ionic strength and pH on the stability of tannic acid-facilitated carbon nanotube suspensions. *Carbon* **47**, 2875-2882 (2009).

46. Ge, D., Yuan, H., Shen, Y., Zhang, W. & Zhu, N. Improved sludge dewaterability by tannic acid conditioning: Temperature, thermodynamics and

684 mechanism studies. *Chemosphere* **230**, 14-23 (2019).

685 47. Yi, Z. et al. Green, effective chemical route for the synthesis of silver nanoplates
686 in tannic acid aqueous solution. *Colloids and Surfaces A: Physicochemical and*
687 *Engineering Aspects* **392**, 131-136 (2011).

688 48. Dultz, S., Mikutta, R., Kara, S.N.M., Woche, S.K. & Guggenberger, G. Effects
689 of solution chemistry on conformation of self-aggregated tannic acid revealed
690 by laser light scattering. *Sci Total Environ* **754**, 142119 (2021).

691 49. Han, Y. et al. Polyphenol-Mediated Assembly of Proteins for Engineering
692 Functional Materials. *Angew Chem Int Ed Engl* **59**, 15618-15625 (2020).

693 50. Lemke, T., Stingl, U., Egert, M., Friedrich, M.W. & Brune, A. Physicochemical
694 conditions and microbial activities in the highly alkaline gut of the humus-
695 feeding larva of Pachnoda ephippiata (Coleoptera: Scarabaeidae). *Appl Environ*
696 *Microbiol* **69**, 6650-6658 (2003).

697 51. Yao, M. & Li, L. (NATIONAL UNIVERSITY CORPORATION
698 HOKKAIDO UNIVERSITY 2022).

699 52. Kabsch, W. Xds. *Acta Crystallogr D Biol Crystallogr* **66**, 125-132 (2010).

700 53. Yu, J., Shinoda, A., Kato, K., Tanaka, I. & Yao, M. A solution-free crystal-
701 mounting platform for native SAD. *Acta Crystallogr D Struct Biol* **76**, 938-945
702 (2020).

703 54. Adams, P.D. et al. PHENIX: a comprehensive Python-based system for
704 macromolecular structure solution. *Acta Crystallogr D Biol Crystallogr* **66**,

705 213-221 (2010).

706 55. Afonine, P.V. et al. Towards automated crystallographic structure refinement
707 with phenix.refine. *Acta Crystallogr D Biol Crystallogr* **68**, 352-367 (2012).

708 56. Emsley, P. & Cowtan, K. Coot: model-building tools for molecular graphics.
709 *Acta Crystallogr D Biol Crystallogr* **60**, 2126-2132 (2004).

710 57. McCoy, A.J. et al. Phaser crystallographic software. *J Appl Crystallogr* **40**, 658-
711 674 (2007).

712 58. Lee, S. et al. Structures of beta-klotho reveal a 'zip code'-like mechanism for
713 endocrine FGF signalling. *Nature* **553**, 501-505 (2018).

714 59. Sastry, G.M., Adzhigirey, M., Day, T., Annabhimoju, R. & Sherman, W. Protein
715 and ligand preparation: parameters, protocols, and influence on virtual
716 screening enrichments. *Journal of Computer-Aided Molecular Design* **27**, 221-
717 234 (2013).

718 60. Wang, Y.L. et al. PubChem: a public information system for analyzing
719 bioactivities of small molecules. *Nucleic Acids Research* **37**, W623-W633
720 (2009).

721 61. Labourel, A. et al. The beta-glucanase ZgLamA from Zobellia galactanivorans
722 evolved a bent active site adapted for efficient degradation of algal laminarin. *J*
723 *Biol Chem* **289**, 2027-2042 (2014).

724

725 Fig 1

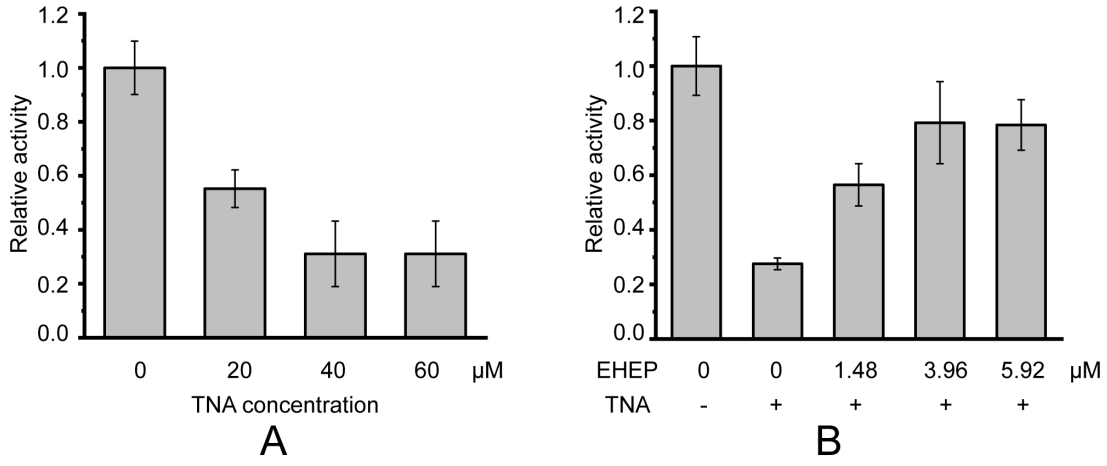

726

727 **Figure 1.** Galactoside hydrolytic activity of *aku*BGL toward ortho-Nitrophenyl-β-
728 galactoside. (A) The hydrolytic activity of akuBGL with TNA at different
729 concentrations. (B) The hydrolytic activity of akuBGL (0.049 μM) with 40 μM TNA
730 and EHEP at different concentrations. The average and standard deviation of the
731 relative activity were estimated from three independent replicates (N = 3).

732 Fig 2

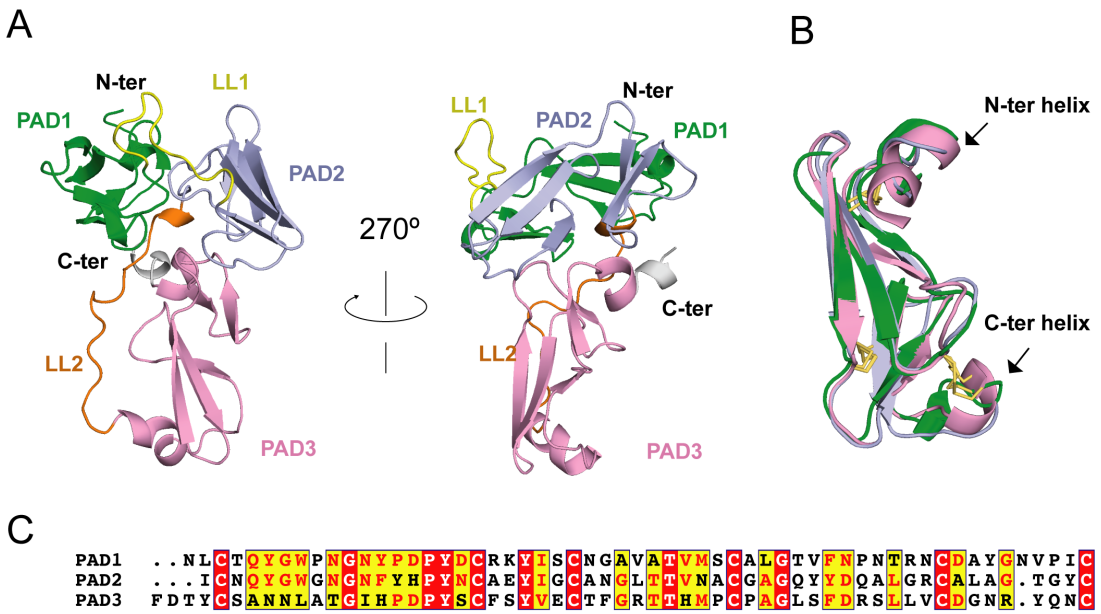

733

734 **Figure 2.** EHEP structure. (A) Cartoon representation of EHEP. The three PAD

735 domains are colored green, light blue, and pink, respectively. Linker long loop1 (LL1)

736 and loop2 (LL2) are colored yellow and blue. (B) Structural superposition of the three

737 PAD domains of EHEP. The three domains are colored as in (A). The disulfide bonds

738 are shown as yellow sticks. (C) Sequence alignment of three PAD domains. Alignment

739 was performed by CLUSTALW and displayed with ESPript3.

740 Fig 3

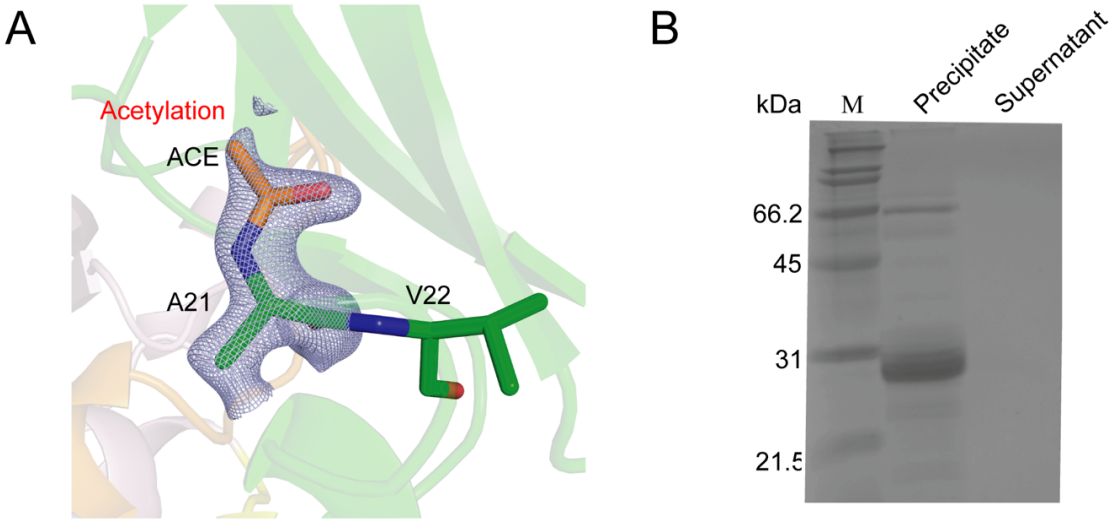

741

742 **Figure. 3**. (A) Acetylation modification on the N-terminal residue A21. The structure

743 is shown as sticks with an omitted map of A21-ace at a 3.3 σ level (blue-white). (B)

744 TNA binding activity of recombEHEP. SDS–PAGE was run using a mixture of

745 recombEHEP and TNA.

746

747 Fig 4

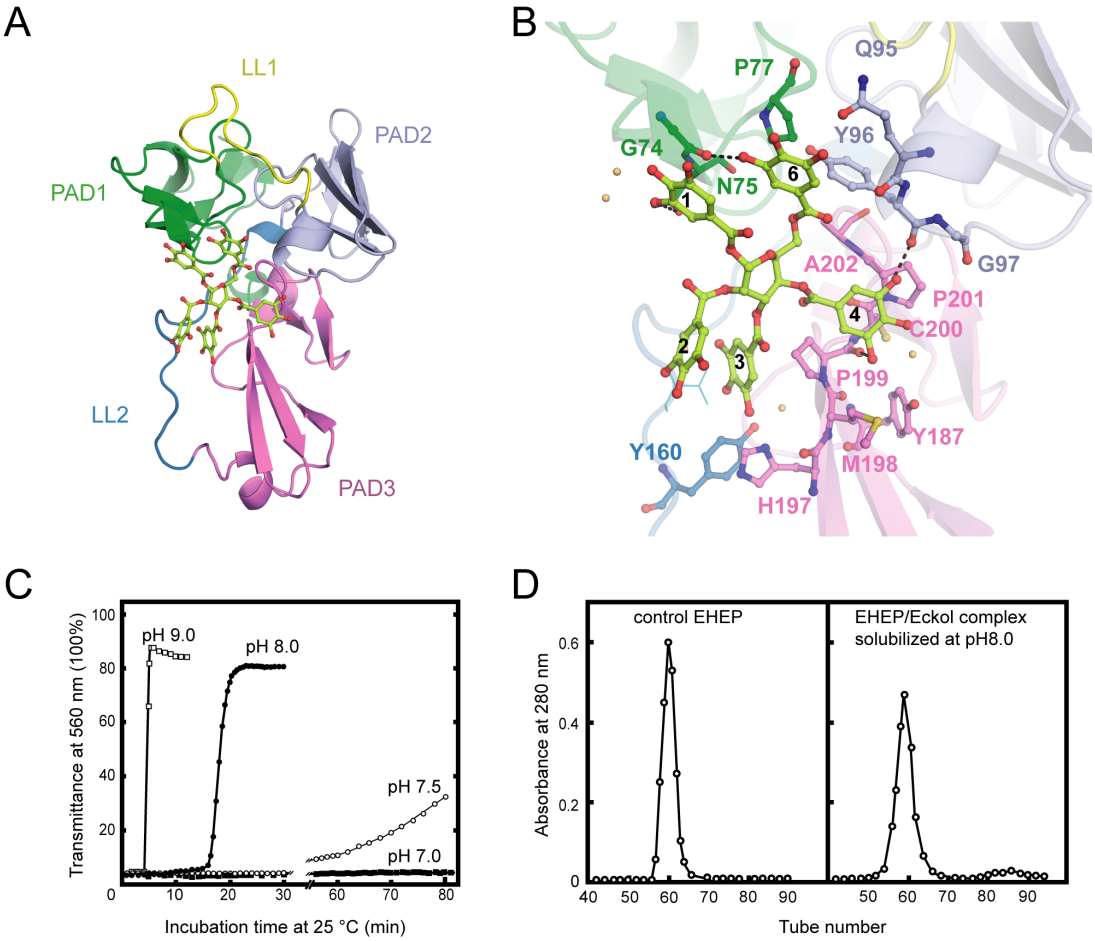

748

749 **Figure 4.** Structure of EHEP-TNA. (a) The overall structure of EHEP-TNA. (A) the

750 overall structure of EHEP-TNA. EHEP and TNA are shown by the cartoon and stick

751 model, respectively. EHEP is colored as in Fig. 1. The C and O atoms of TNA are

752 colored lemon and red, respectively. (B) Interaction of TNA (ball-stick in same color

753 as (A)) with EHEP (cartoon in same color as (A)) in EHEP-TNA structure. The residues

754 of EHEP in contact are labeled and shown by a ball-stick with N, O, and S atoms in

755 blue, red, and brown, respectively. The C and O atoms of TNA are colored the same as

756 (A), lemon and red, respectively. Dashed lines show hydrogen bonds. The water

757 molecules stabilizing TNA was shown as light orange spheres. (C) Effect of pH on

758 resolubilization of an EHEP–eckol precipitate. Buffers with pH 9.0, 8.0, 7.5, and 7.0

759 are presented as hollow square, solid circle, hollow circle, and solid square, respectively.

760 (D) The EHEP–eckol precipitate was dissoloved in 50 mM Tris–HCl (pH 8.0) and

761 analyzed by Sephacryl S-100.

762

763 Fig 5

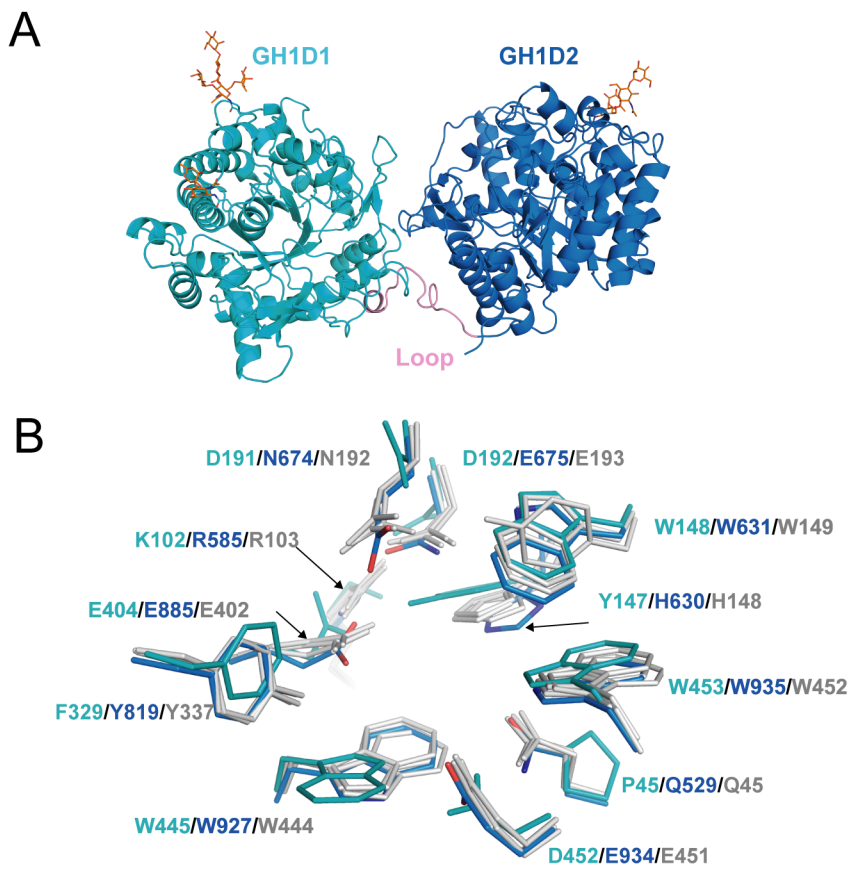

764

765 **Figure 5.** Structure of *aku*BGL. (A) Overall structure. The GH1D1 (light blue) and

766 GH1D2 (cyan) domains are linked by a long loop (linker-loop) colored in pink. The N-

767 linked glycans were shown in the orange stick. (B) Residues superposition of the GBS

768 and CR sites of the domains GH1D1 (cyan), GH1D2 (light blue) with β-glucosidase

769 structures from termite *Neotermes koshunensis* (*Nk*BGL, grey), β-glucosidase from rice

770 (*Os*BGL, gray), β-glucosidase from *Bacillus circulans* sp. *Alkalophilus* (grey). Only the

771 residues numbers of GH1D1 (cyan), GH1D2 (light blue), and *Nk*BGL (grey) are shown

772 for clarity.

773

774 Fig 6

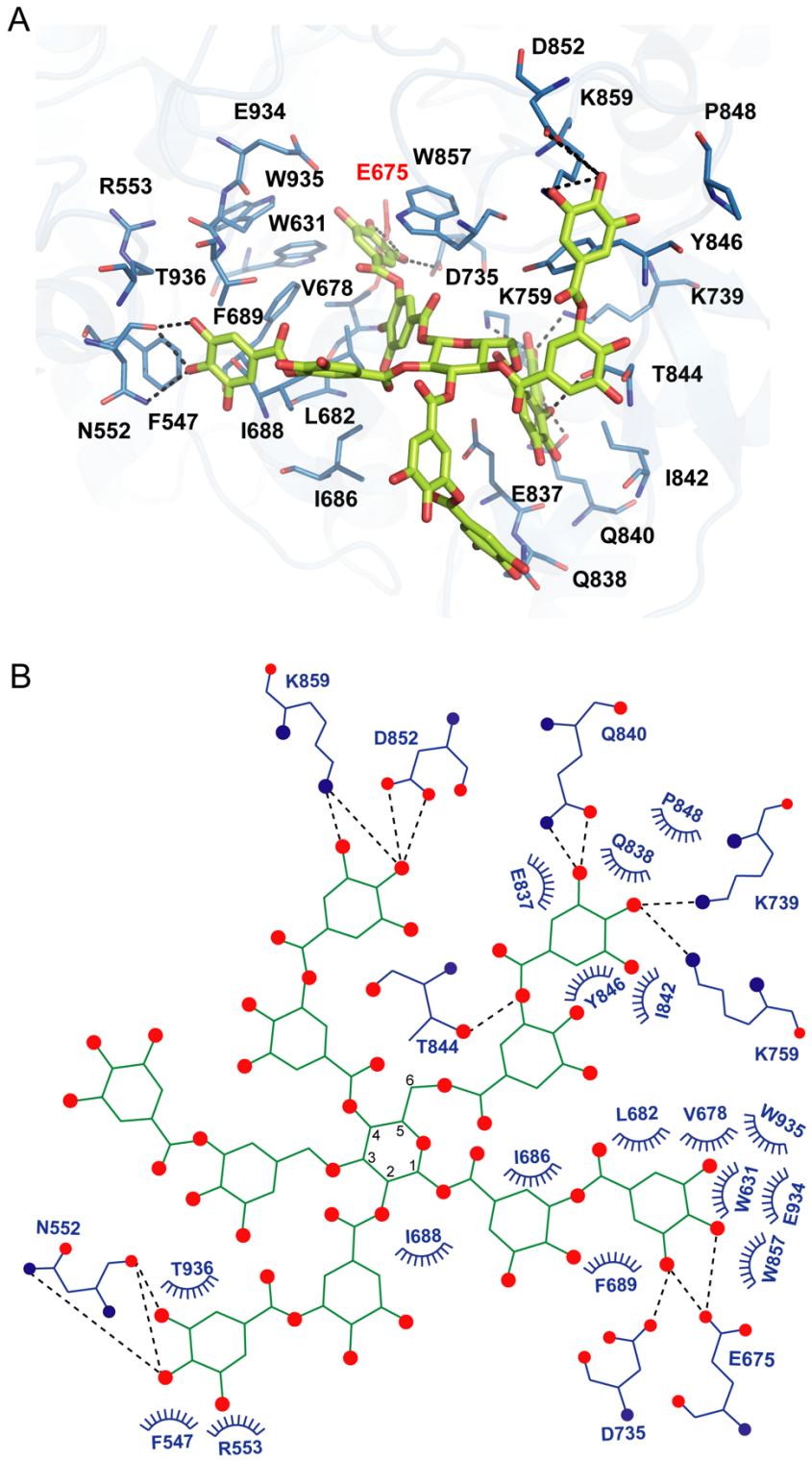

775

776 **Figure 6.** Docking model of *aku*BGL with TNA. (A) Detailed interaction between

777 *aku*BGL and TNA in the docking model. TNA is shown in the green stick model. The

778 hydrogen bonds are shown as dashed lines. (B) A 2D diagram of the interaction between

779 *aku*BGL and TNA shown in (A). The hydrogen bonds are shown as dash lines, and the

780 hydrophobic contacts as circular arcs.

781 Fig 7

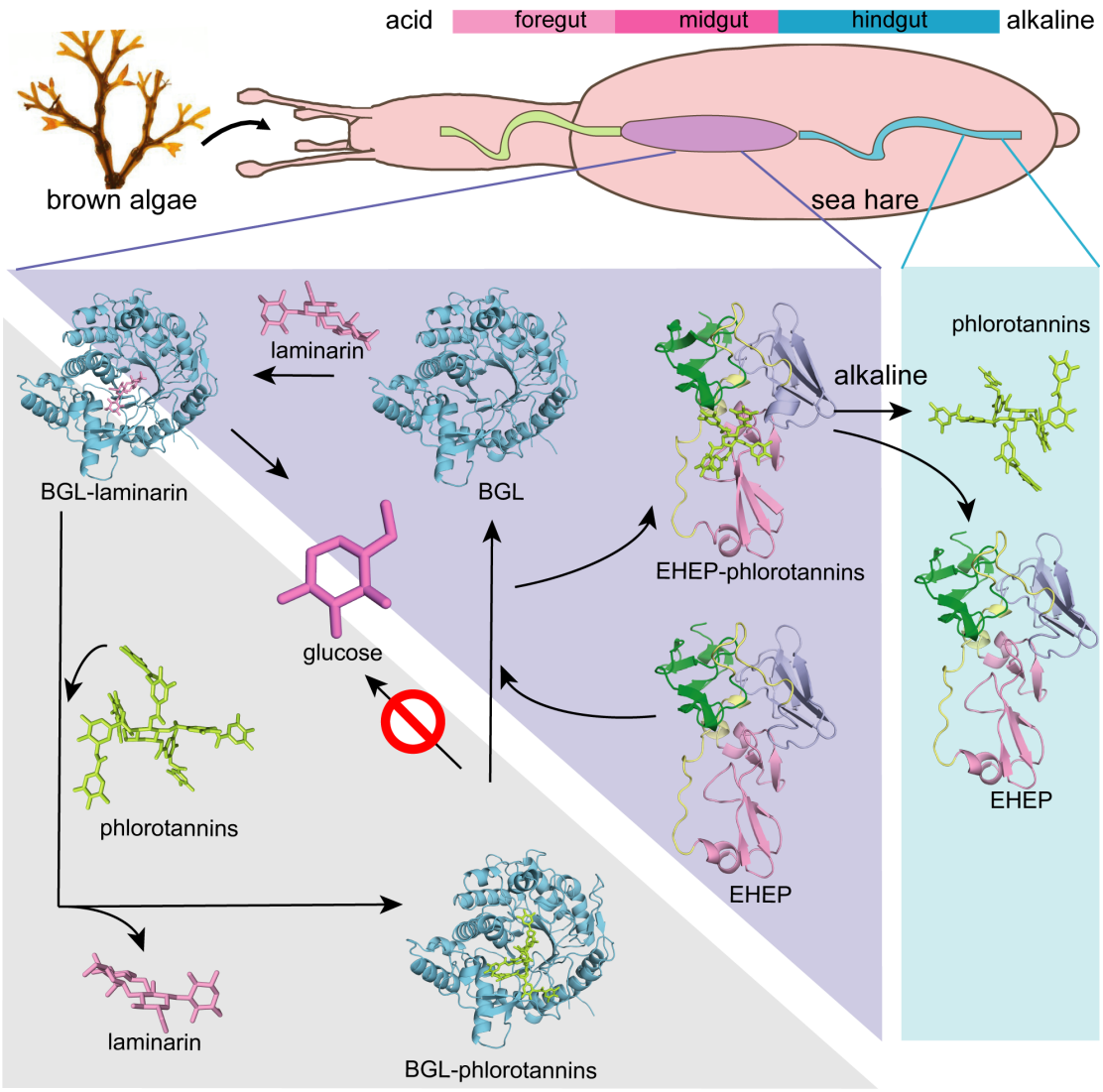

782

783 **Figure 7.** Proposed molecular mechanisms. Proposed molecular mechanisms of TNA

784 inhibition of *aku*BGL activity and EHEP's protective effects of *aku*BGL in *aku*BGL–

785 phlorotannin/laminarin–EHEP system (light purple triangle). The digestive tract of

786 *A.kurodai* consists of foregut (blue), midgut (purple), and hindgut (blue) (top). The bar

787 chart above depicts the pH of the digestive tract, with pink denoting acid and blue

788 denoting alkalinity.

789

790 **Table 1** X-ray data collection and structure-refinement statistics.

	Native-SAD of EHEP	EHEP1	EHEP2	EHEP-TNA	*aku*BGL
Data Collection					
Beamline	PF BL17A	PF BL17A	Spring 8 BL-41XU	PF BL17A	PF BL1A
Wavelength (Å)	2.1000	0.9800	1.0000	0.9800	1.0000
Resolution range (Å)	46.61-2.48 (2.54-2.48)	46.56–1.15 (1.20–1.15)	47.02- 1.4 (1.45-1.4)	46.84–1.9 (1.97–1.9)	49.65-2.7 (2.80-2.7)
Space group	$P2_12_12_1$	$P2_12_12_1$	$P2_12_12_1$	$P2_12_12_1$	$P6_2$
Unit-cell parameters *a, b, c* (Å)	42.2, 65.3, 66.5	42.2, 65.3, 66.5	40.6, 65.6, 67.5	42.5, 65.4, 67.2	191.7, 191.7, 112.6
Completeness (%)	97.7 (87.5)	93.4 (75.8)	99.30 (97.98)	99.9 (99.7)	99.9 (99.1)
Redundancy	99.7 (38.9)	6.6 (6.1)	6.4 (5.8)	6.4 (6.4)	10.7 (10.9)
Average I/σ(I)	105.1 (74.4)	19.28 (1.97)	14.34 (3.41)	15.39 (1.83)	10.69 (2.57)
R_{meas}(%)[a]	6.9 (14.2)	7.3 (90.5)	8.6 73.7(55.3)	8.9 (89.4)	19.4 (83.0)
$CC^{1/2}$ (%)	100 (99.8)	99.9（70.4）	99.8 (86.2)	99.9（73.7）	99.5 (84.2)
Ano/Sig	3.1 (1.7)				
Molecules/ asymmetric unit	1	1	1	1	2
Refinement					
R_{work}[b]/R_{free}[c] (%)		18.19/18.91	16.57/18.39	19.87/23.54	18.39/21.98
No. of atoms		1955	1861	1732	15595
No. of residues		1600	1573	1580	15256
No. of water molecules		343	273	87	96
No. of Ligands		12	15	67	243
RMSD from ideality					
bond length (Å)		0.005	0.006	0.008	0.004
bond angle (°)		0.84	0.84	0.91	0.65
Ramachandran plot (%)					

Favoured	99.02	98.54	98.52	96.16
Allowed	0.98	1.46	1.48	3.74
Outliers	0.00	0.00	0.00	0.11
PDB accession code	8IN3	8IN4	8IN6	8IN1

The highest resolution shell is shown in parentheses.

[a]$R_{meas} = \Sigma_{hkl}\{N(hkl) / [N(hkl) -1] \}^{1/2} \Sigma_i|I_i(hkl)-< I(hkl)> | /\Sigma_{hkl} \Sigma_i|I_i(hkl)$, where where $I_i(hkl)$ is the ith observation of the intensity of reflection *hkl* and $\langle I(hkl)\rangle$ is the mean over n observations.

[b]$R_{work} = \Sigma_{hkl}||F_{obs}(hkl)| - |F_{calc}(hkl)||/\Sigma_{hkl}|F_{obs}(hkl)|$.

[c]R_{free} was calculated with an approximate 5% fraction of randomly selected reflections evaluated from refinement.

799 **Supporting information**

800 Fig.S1

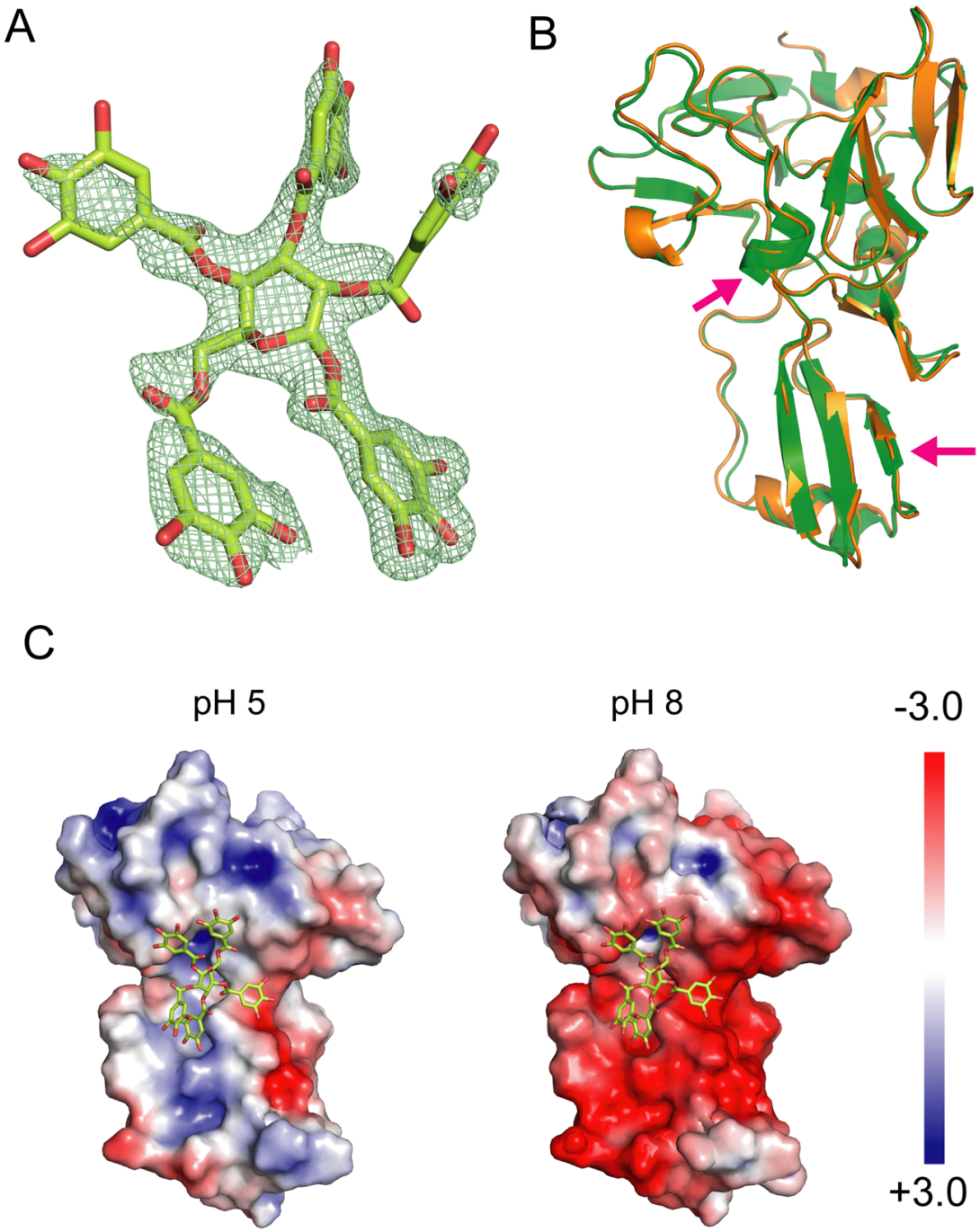

801

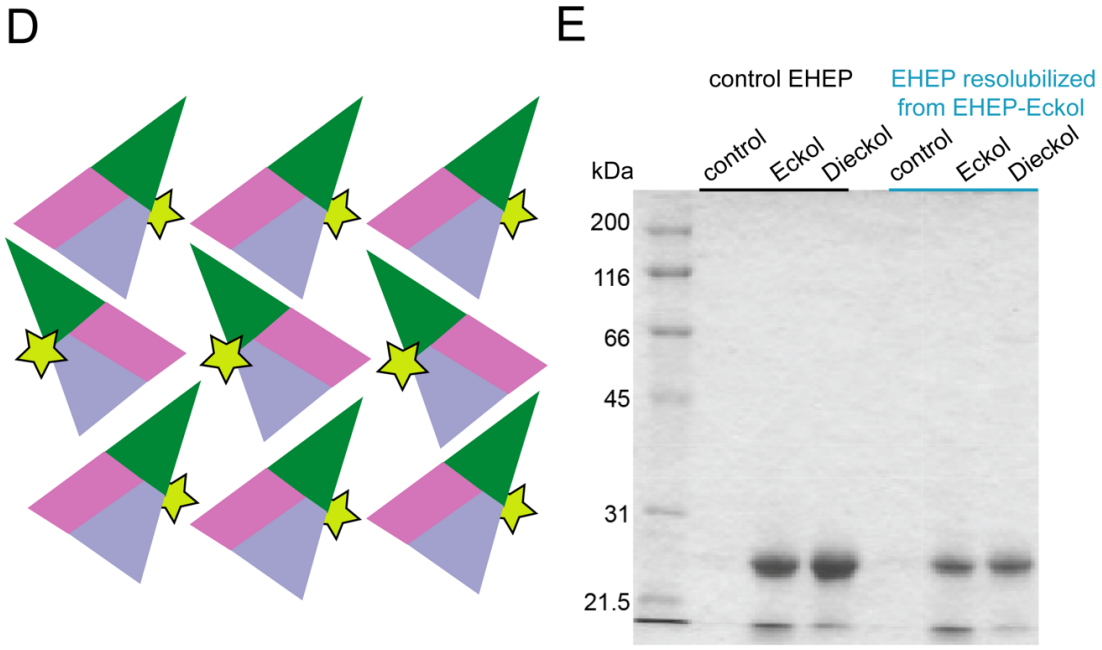

Figure S1. EHEP–TNA structure and structural comparisons. (A) TNA structure (stick model) in EHEP–TNA with an omitted map countered at the 2.0 σ level. The O and C atoms are colored red and lemon, respectively. (B) Structure superposition of apo EHEP (orange) with EHEP–TNA (green). Two arrows mark the conformational changes in a β-sheet of PAD1 and an α-helix of PAD2, respectively. (C) Electrostatic potential of the EHEP surface in the EHEP–TNA complex at different pH values. (D) Diagram of EHEP–TNA packing in the crystal structure. The triangle represents the EHEP, with the three colors denoting the three PAD domains, as in Fig. 3a. TNA is shown in a lemon pentagram. (E) Activity of the resolubilized EHEP. The EHEP-eckol precipitate was resolubilized in Tris–HCl (pH 8.0) and then the supernatant was purified by Sephacrys S-100 column to measure eckol-binding activity.

Fig.S2

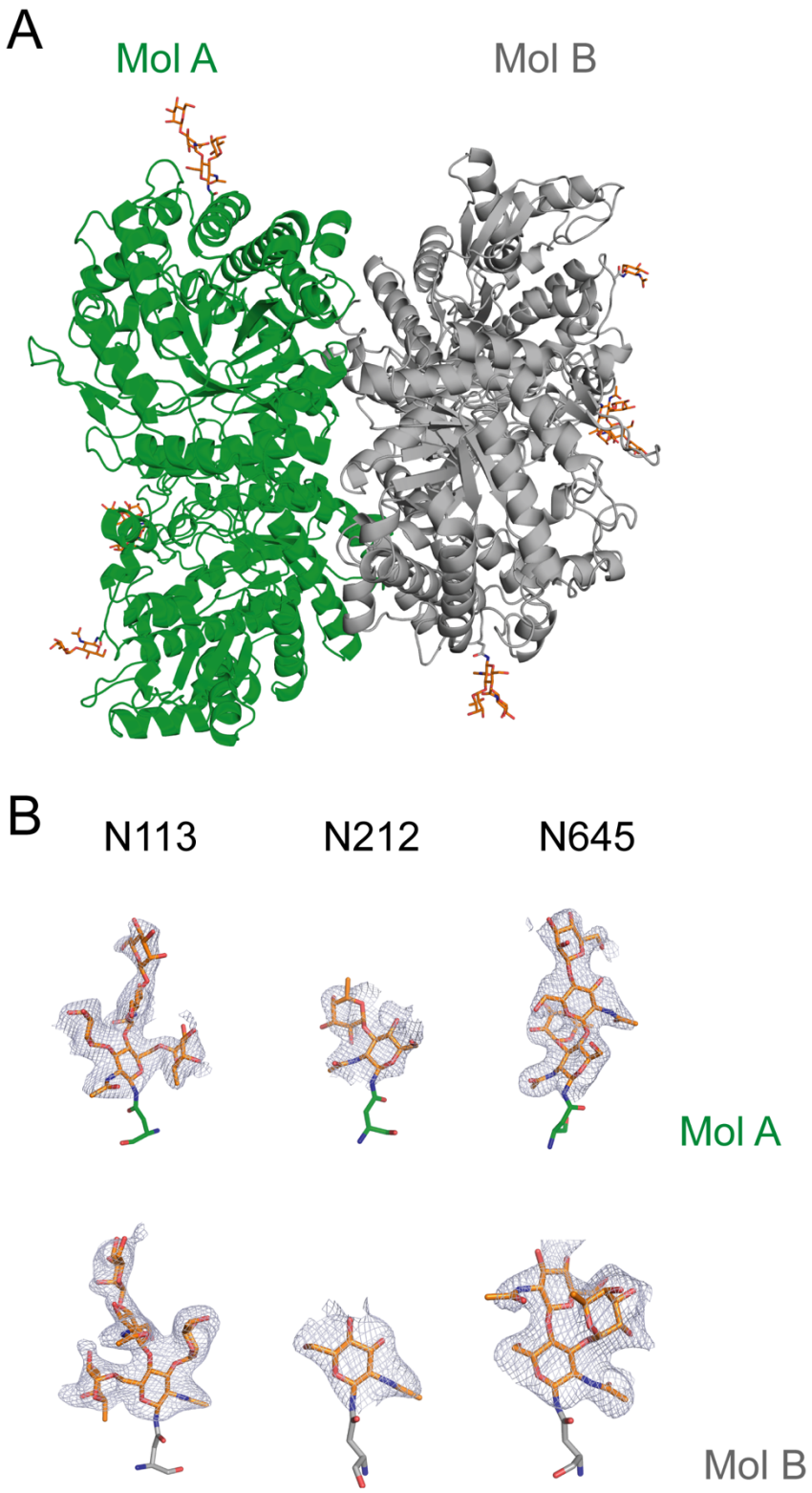

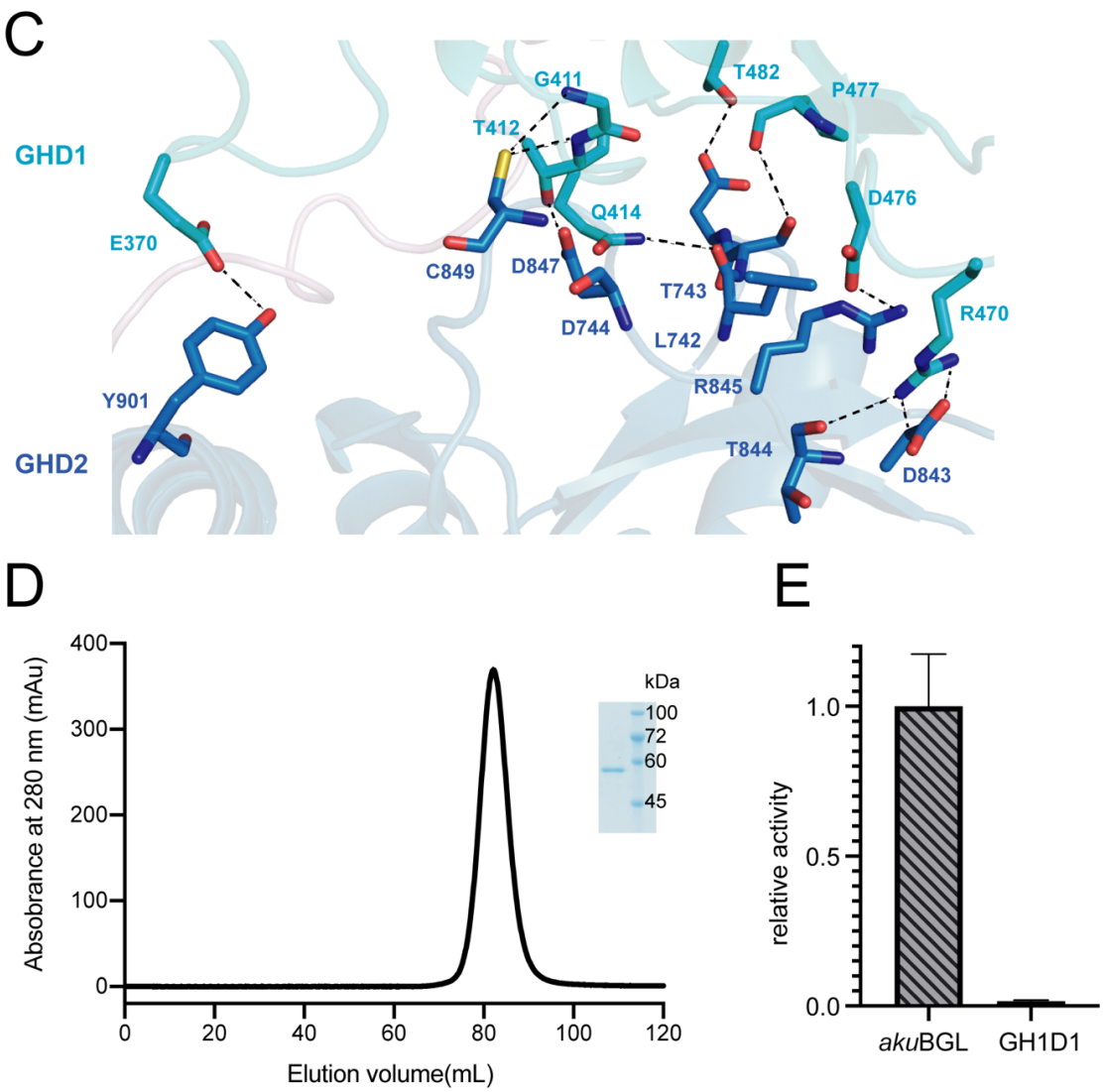

Figure S2. *aku*BGL structure. (A) Two *aku*BGL molecules in the asymmetry unit, colored green and grey, respectively. The glycosylation sites are shown as orange sticks, with O and N atoms in red and blue, respectively. (B) The glycosylation chains with omitted density maps are countered at the 2.0 σ level. (C) The interface between the GH1D1 (cyan) and GH1D2 (blue). The key interactions between the two domains are shown as black dashed lines. (D) Size exclusion chromatogram of the purified GH1D1 domain. The inset shows the SDS–PAGE analysis of the GH1D1 domain. (E) Galactoside hydrolytic activity of the GH1D1 toward ortho-Nitrophenyl-β-galactoside.

826 The average and standard deviation of the relative activity were estimated from three

827 independent replicates (N = 3).

828 Fig. S3

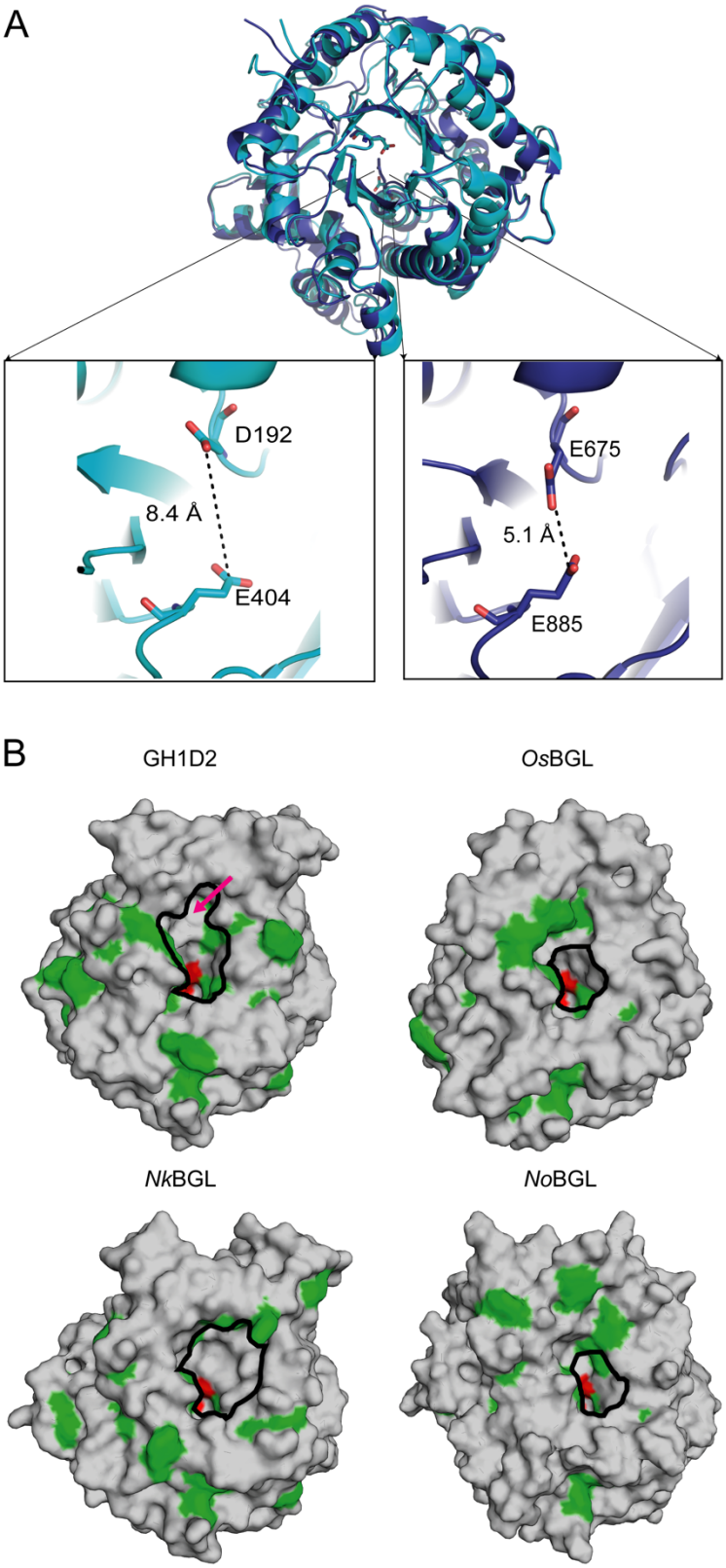

829

830 **Figure S3.** Structural comparison of BGLs. (A) Structure superposition of

831 GH1D1(cyan) and GH1D2 (blue). The enlarged picture shows the distance of
832 conceivable catalytic residues in GH1D1 and GH1D2. (B) Surface representations of
833 GH1D2, *Nk*BGL, *Os*BGL, and *No*BGL with the aromatic and catalytic residues colored
834 green and red, respectively. The red arrow indicates the location of the auxiliary site of
835 GH1D2. The active pockets are highlighted by a black circle on each surface.

836 **Fig. S4**

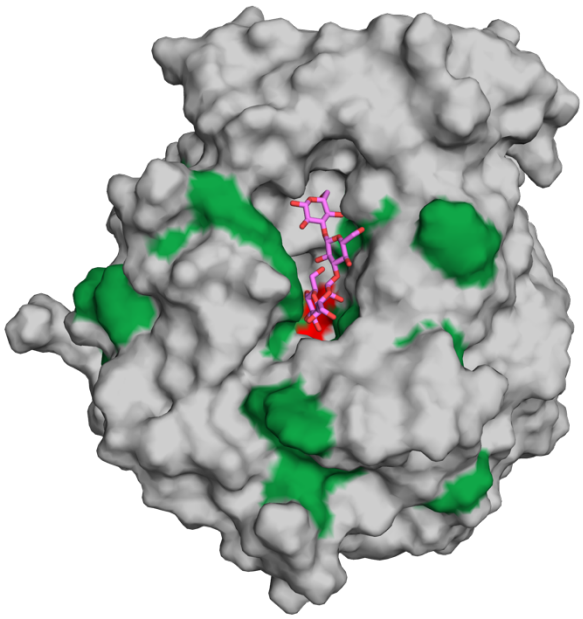

837

838 **Figure S4.** The model of GH1D2 docking with the substrate laminaritetraose. GH1D2
839 is shown as a grey surface representation and laminaritetraose as marine sticks. The
840 aromatic and catalytic residues of GH1D2 are colored green and red, respectively.

841

842 Fig. S5

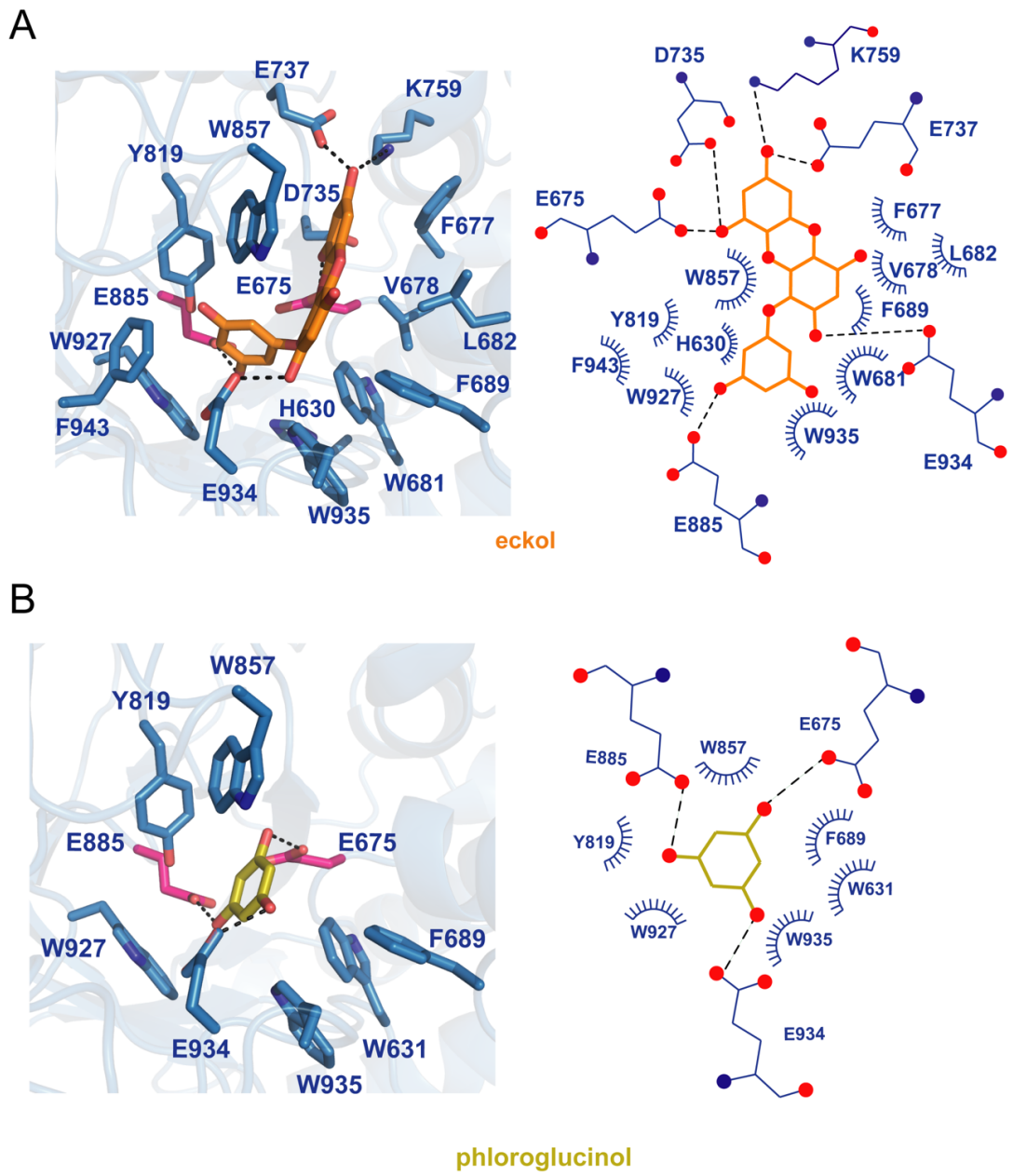

843

844 **Figure S5.** The models of GH1D2 docking (A) With eckol; (B) With phloroglucinol.

845 The left panel shows the 3D structures, and the right panel shows the 2D diagrams. The

846 C, N, and O atoms of residues are colored light blue, dark blue, and red, respectively.

847 The C atoms of eckol and phloroglucinol are shown in orange and yellow, respectively.

848